Development of Modal Analysis for the Study of Global Modes in High Speed Boundary Layer Flows

A DISSERTATION
SUBMITTED TO THE FACULTY OF THE GRADUATE SCHOOL
OF THE UNIVERSITY OF MINNESOTA
BY

Joseph Michael Brock

IN PARTIAL FULFILLMENT OF THE REQUIREMENTS
FOR THE DEGREE OF
Doctor of Philosophy

Graham V. Candler, Advisor

May, 2017

Acknowledgements

The work presented in this dissertation represents the study, work, and experience over the past 8 years as a student at the University of Minnesota. The majority of my success is owed to the many individuals, whom I have had the pleasure of meeting and working with over the course of "extended" graduate career. I would like to take a moment to recognize them now.

I must first thank Doctor Darrel F. Untereker. His taking a chance on me as a young intern at Medtronic, and continued mentoring was most certainly the transitioning point in my life. I arrived at Medtronic with an interest in science, and left with an obsession. I cannot thank him enough for having faith and pushing me to continue my studies, leading to my application to graduate school. I owe my appreciation for science and research to his influence.

I must thank my advisor, Professor Graham Candler, for also taking a chance on me so early on in my academic career. His influence, expertise, and will to always be learning has been inspirational over the years. I am hopeful that this work lives up to his expectations and am truly honored to have an association with such a successful and respected expert.

Much of this work was motivated by the many discussions with Professor Mihailo Jovanovic. His expertise in the complicated mathematical concepts and his willingness to guide me through the details to the big picture implications of this work is very

appreciated. I am very grateful for all of his help and guidance.

I must thank Professor Joseph Nichols for his incredible amount of expertise and enthusiasm for this work. The many one-on-one sessions and countless emails show his professionalism and greatness as a teacher. I am grateful for his seemingly endless patience and continued help throughout all of this work.

I consider Doctor Pramod Subbareddy to be one of personal advisors, and a great friend. I am very appreciative of his tenacity in research and compassion in personal relationships. I owe much of my success along the way to his teachings and insight. I will forever appreciate the academic help and personal breaks which helped me keep my sanity.

I am grateful to the people in Graham's research group at the University of Minnesota. The many students that are part of Graham's research group are some of the best, brightest, and most friendly people I have ever had the pleasure of working with. I must thank; Ioannis Nompelis, Matt Bartkowicz, Ross Wagnild, Dave Peterson, Travis Drayna, Heath Johnson, Pietro Ferrero, Vladimyr Gidzak, Erik Tylczak, Loretta Trevino, Kyle Boe, Jason Bender, Alan Schwing, Aaron Neville, Stephanie Jenson, Ross Chaudhry, Sidharth GS, Anand Kartha, and Jeffrey Komives. A special thank you to Derek Dinzl for all of the late nights, early lunches, and countless hours discussing life and transition. Finally, to my best friend throughout my entire graduate career, Eric Stern, I must extend a very special thank you. From the early days of hipster living and pizza, to the later lessons in billiards, wine, politics, and life, I have always appreciated and been thankful for our friendship. I have great respect for your professionalism and greatness. Here is to many more years of friendship with all of you.

Finally, and most importantly, I would like to thank my family. To my father and roll model, Michael Brock; my mother, an unyielding pillar of support, Laura Brock; my sister and greatest ally, Heather Brock, I thank all of you. This could not have been done without you. To my amazing wife, Stefanie, for her endless patience, support, and

my constant motivation. My family is my greatest gift and I love you all.

Dedication

For my amazing wife, Stefanie.

Abstract

Boundary layer transition for compressible flows remains a challenging and unsolved problem. In the context of high-speed compressible flow, transitional and turbulent boundary-layers produce significantly higher surface heating caused by an increase in skin-friction. The higher heating associated with transitional and turbulent boundary layers drives thermal protection systems (TPS) and mission trajectory bounds. Proper understanding of the mechanisms that drive transition is crucial to the successful design and operation of the next generation spacecraft.

Currently, prediction of boundary-layer transition is based on experimental efforts and computational stability analysis. Computational analysis, anchored by experimental correlations, offers an avenue to assess/predict stability at a reduced cost. Classical methods of Linearized Stability Theory (LST) and Parabolized Stability Equations (PSE) have proven to be very useful for simple geometries/base flows. Under certain conditions the assumptions that are inherent to classical methods become invalid and the use of LST/PSE is inaccurate. In these situations, a global approach must be considered.

A TriGlobal stability analysis code, Global Mode Analysis in US3D (GMAUS3D), has been developed and implemented into the unstructured solver US3D. A discussion of the methodology and implementation will be presented. Two flow configurations are presented in an effort to validate/verify the approach. First, stability analysis for a subsonic cylinder wake is performed and results compared to literature. Second, a supersonic blunt cone is considered to directly compare LST/PSE analysis and results generated by GMAUS3D.

Contents

List of Tables

List of Figures

Chapter 1

Introduction

1.1 The Transitional Boundary Layer

A primary concern for hypersonic vehicle design is aerodynamic heating the vehicle experiences due to the skin friction imposed by the attached near wall region known as the boundary layer. The levels of skin friction for a turbulent boundary layer are higher compared to laminar boundary layers, resulting in an increase of the heat flux at the surface of the vehicle. The mechanisms responsible for transition in high-speed compressible flow are not fully understood. Due to a poor understanding of the many mechanisms by which a boundary layer may become turbulent, many engineering designs of thermal protection systems (TPS) employ conservative margins. This results in additional weight added to the vehicle, which affects the payload margins, stability characteristics in flight, as well as fuel required during ascent and descent. Proper understanding and characterization of the mechanisms responsible for laminar-turbulent transition will help counter the negative side-effects on high-speed vehicle design. For engineering purposes, the boundary layer can be characterized as one of three states; laminar, turbulent, or transitional.

The laminar boundary layer is aptly named due to fluid having several layers (lamina) of constant flow values (i.e. density, momentum, energy, *etc*) in the wall normal direction with fairly uniform values in the stream- and span-wise direction. Because the flow paths are separated into lamina, any exchange of flow quantities (such as mass or momentum) occurs only through molecular diffusion.

In contrast to the laminar boundary layer, turbulent boundary layers exchange mass and momentum through molecular diffusion as well as mixing produced by chaotic motion of eddies (vortical fluid structures) within the boundary layer. Large scale mixing distributes high-momentum fluid down towards the wall, increasing the wall-normal gradients significantly. Small scale mixing dissipates energy into heat. The effect of large and small scale mixing produces a boundary layer that contains hot high gradient fluid near the wall, which ultimately increases the surface heating.

The state between a laminar and turbulent boundary layer is called transitional. The transitional boundary layer is characterized by the sporadic nature in which a laminar profile is disrupted due to the presence of disturbances. The augmentation of the laminar profile is due to disturbances amplifying to high enough energy levels to affect the steady flow. Once the steady-state is augmented and the boundary layer profile begins to deviate from that of a laminar one, the disturbances and augmented laminar state begin to interact non-linearly. Given sufficient interaction time and/or distance, interactions between the augmented boundary layer profile and amplified disturbances may continue to increase in strength and breakdown to turbulence will occur.

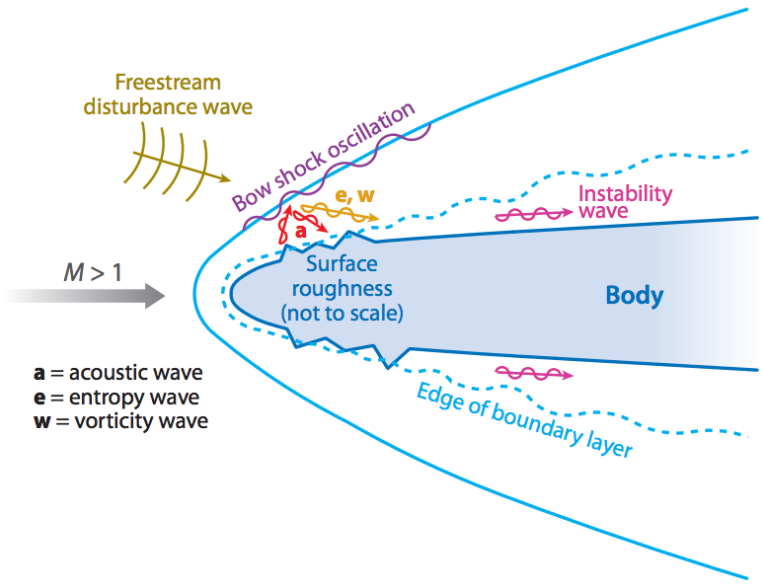

Figure 1.1: Schematic of different environmental forcing types

Figure 1.1, taken from Zhong *et al.* [7], shows a graphical representation of a blunt body in supersonic flow in the presence of free stream and surface disturbance forcing. The region upstream of the solid surface, is dominated by a strong bow shock. Close to the wall, a boundary layer develops due to the effect of a "no slip" condition on the individual fluid molecules and their interaction with the surface. Under supersonic/hypersonic conditions, the interaction of free stream disturbances with the standing bow shock produces entropy, vorticity, and acoustic waves which radiate inwards towards the surface. These disturbance are often referred to as *natural* disturbances. Additionally, surface roughness on the vehicle can contribute to the disturbance forcing. Surface roughness may be characterized as either isolated or distributed. Isolated roughness elements correspond to individual surface features, typically on the order of the boundary layer height (such as bolts, mold lines, etc), while distributed roughness

describes unpolished rough surfaces (such as paint coatings, post ablated surfaces, etc). For small disturbances, the initial interaction with the boundary layer can result in a preferred disturbance type and frequency to be selected and enter the boundary layer region. This is known as the receptivity process and is the first stage in the many paths by which a boundary layer can become turbulent.

1.2 Paths to Transition

Morkovin was the first to simplify all the processes by which transition my occur into a graphical road map [8]. The road map was later edited to include transient growth [9]. The graphical representation of the many paths to transition is shown in Figure 1.2. The top portion of the graphic represents disturbance forcing. The energy of the incoming disturbances can range from small to large levels (depicted by the shaded arrow from left to right). As disturbances are introduced to the boundary layer, a selection process known as receptivity takes place. Receptivity is a physical mechanism by which a preferred disturbance shape and frequency is selected and enters the boundary layer. Due to the convective nature of high-speed boundary layers, the disturbance will travel downstream. The disturbance may amplify or decay depending on the features of the underlying base flow[1] and disturbance type. The individual ways by which a disturbance may amplify is represented by the individual paths *a*-*e*.

[1] The term base flow does not refer to the mean flow. The term mean flow is reserved only to describe time averaged states

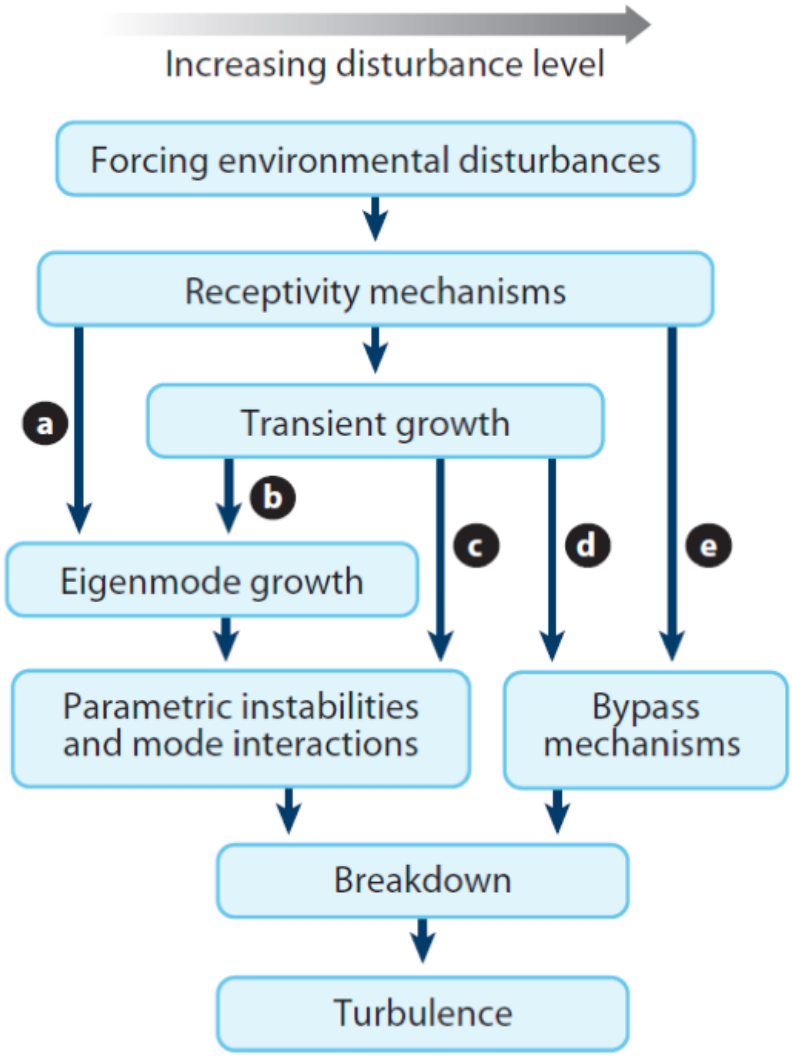

Figure 1.2: Graphic showing the various paths to transition

Path A represents disturbances that are governed by eigenmode [2] growth (1st mode, 2nd mode, Görtler instability, and crossflow instability). These disturbances are able to

[2] The term eigenmode growth corresponds to the fact that the amplification or decay of the disturbance is governed the solutions to an eigenvalue problem. The disturbance shapes themselves are eigenvectors or eigen*modes*.

amplify from infinitesimal amplitudes to amplitudes on the order of the underlying base flow quantities. The influence of these disturbances may lead to an augmentation of the base flow profile. The new, augmented, base state may develop additional instabilities (referred to as secondary instability) that allow additional disturbances to amplify. The amplification of the disturbance to large enough levels to augment the base state and nonlinearly interact with each other can result in the breakdown of laminar profile. The flow eventually develops into a fully turbulent boundary layer shortly thereafter.

Paths B-D represent special cases of disturbance amplification known as transient growth. These disturbances (typically ones that have higher initial amplitudes compared to the Path A disturbances) may interact with one another (linearly) to cause brief periods of disturbance energy amplification. Path B represents a passing of the, now higher in amplitude, disturbances into an unstable region of the flow where their dynamics can be described by eigenmode growth. Path C represents the case in which the energy amplification of the disturbance is significant enough to augment the base flow profile, resulting in secondary instabilities and nonlinear interactions. Finally, path D is the first of the bypass mechanisms. Modes that follow this path typically originate in flows with moderate levels of free stream turbulence. The laminar boundary layer then contains a weak turbulence spectrum of disturbances, which grow significantly. This growth occurs fast enough such that mode-mode interactions and secondary instabilities are 'bypassed' and the laminar base flow breaks down purely due to the fluctuations of these disturbances.

Path E represents free stream disturbance levels so large that disturbance amplification leads directly to bypass mechanisms. These situations are likely due to strong free stream turbulence.

1.3 Historical Overview of Transition Research

The entire history of hydrodynamic stability is vast and can arguably be dated back to the early drawings of Leonardo De Vinci where he illustrated complex patterns in the wakes of rocks in a stream. Since that time, many have sought to explain the dynamic behavior of fluids in all regimes. While there have been many accomplishments, discoveries, and theory formation/alterations throughout the years, only a brief overview of a few historical milestones will be given here. For a more thorough explanation of each of the discoveries, the reader is referred to the cited works within this chapter.

Published work on the study of hydrodynamic stability and transition starts with the early experimental studies of Reynolds[10]. The results of these experiments produced one of the first non-dimensional parameters (the Reynolds number: Re) intended as a criterion of stability. Flows whose Reynolds number were below some critical value were deemed stable while flows that exceeded the critical value were characterized as unstable. The non-dimensional parameter (Re) is still used today as a broad characterization of flow regime and many non-dimensional parameters are related to or based off of the Reynolds number.

Early numerical analysis of hydrodynamic stability relied on heavily simplified assumptions of the underlying base flow in addition to asymptotic behavior of the dynamics [11]. The first formulation of the viscous stability problem was by Orr in 1907 [12], followed by Sommerfeld in 1908 [13]. The result of which led to the famous Orr-Sommerfeld equations which describe locally parallel incompressible viscous flow. However, it would take over 60 years for numerical analysis using the Orr-Sommerfeld equations to first be performed by Orzag in 1971 [14]. The Orr-Sommerfeld equations provided new insight which led to many physical discovers such as the prediction and discover of Taylor rolls in 1929[15].

Numerical analysis continued to increase in complexity and the discovery of fundamental mechanisms followed. The first theoretical prediction of viscous instabilities for incompressible boundary layers were known as Tollmien-Schlichting waves, named after Tollmein 1929 [16] and Schlichting 1933 [17]. Experimental observation of T-S waves didn't occur until 1962 by Klebanoff *et al.* [18]. The extension of T-S waves and discovery of additional disturbances in the compressible boundary layer is attributed to the work by Mack in 1963 [19].

The fist derivation of the mathematical framework for spatial stability analysis was performed by Gaster in 1964 [20]. In 1976 Joseph defined bounds on maximum energy growth within boundary layers [21].

Secondary instabilities, as they relate to T-S waves, were discovered by Orszag and Patera in 1983 [22]. Elliptical instabilities were discovered by Bayly [23], and Pierrehumbert [24] in 1986.

Absolute instabilities were first described by the works of Huerre and Monkewitz in 1990 [25].

Finally, the derivation of the Parabolized Stability Equations (PSE) was put forth in 1992 by Bertolotti [26] and first applied by Chang and Malik in 1994 [27]. The use of the PSE has since become very popular in the stability analysis of high speed boundary layers for simple geometries. Today, PSE and linear stability analysis (LST) are the main approaches when preforming stability analysis.

1.4 Motivation for Current Research

Given the long history and advancements in the study of hydrodynamic stability, there is still much to learn about the vast field of boundary layer transition. Much of the computational analysis is performed using the classical approaches of LST and PSE.

These computational tools, when used alongside experimental/flight observations, provide excellent *a priori* characterization of high speed boundary layers. While these approaches are computationally efficient, and have been verified and validated against many different flow regimes, the underlying mathematical assumptions can break down resulting in poor or incorrect predictions.

Transition prediction using LST and PSE rely on the e^N method[28]. An overview of the e^N method is available by Reed *et al.*[29]. The total growth of a disturbance "N-factor", as computed by LST/PSE, is compared to an empirically obtained quantity (typically based on some set of experiments). When the growth exceeds the values from experimental observations, transition is said to occur.

The study of boundary layer transition performed by Gosse [1] *et al.* on the Hypersonic International Flight Research Experimentation 5 (HIFiRE 5) shows a specific example where LST and PSE can produce poor stability estimations. Figure 1.3 shows the base flow contours of the elliptic cone geometry for HIFiRE 5. The bottom edge of the cone is referred to as the attachment line, while the top of the image (near the symmetry plane) is referred to as the centerline. Due to the asymmetry in the azimuthal direction, the fluid flow around the cone produces a three-dimensional boundary layer profile. This profile results in the production of a "crossflow" profile. At the leading edge of the geometry the boundary layer is thin and attached, while at the centerline of the geometry, the boundary layer is lifted and often separated due to the coalescence of fluid from the influence of crossflow velocity profiles pushing fluid toward the centerline.

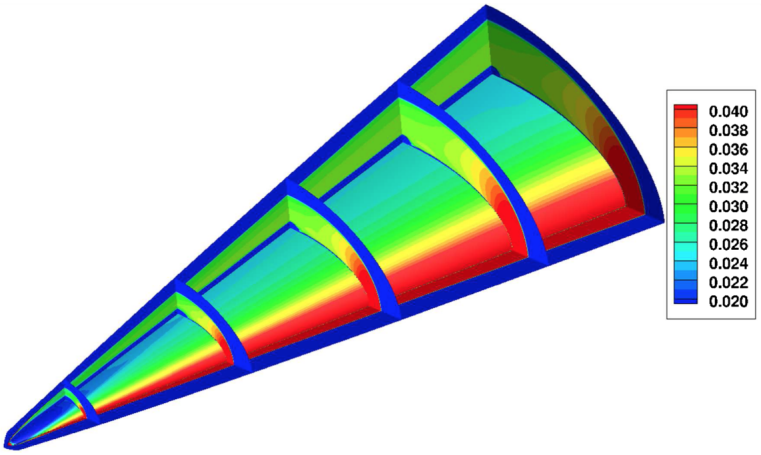

Figure 1.3: International Flight Research Experimentation 5 (HIFiRE 5) geometry with contours of fluid density. Gosse [1]

Gosse *et al.* performed LST and PSE analysis on the leading edge as well as the centerline of the geometry. Figures 1.4 (a)-(d) show the results for LST and PSE analysis for the leading edge and centerline planes. The red, orange, and purple lines represent the results obtained by LST as estimations for the maximum amplification for a given frequency. The contours are the solutions obtained by PSE. The black line in each plot is the maximum N-factor frequency curve. This curve represents the envelope over all frequencies and is the total N-factor. What is important to note is the relative smoothness in the solutions between (a) the leading edge as compared to (b) the centerline plane. This is due to the lifted boundary layer providing difficulty for the solver due to a breaking of the underlying assumptions inherent in the mathematical approaches.

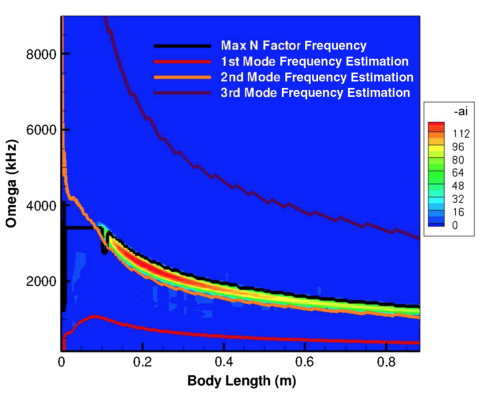

(a) LST results for leading edge

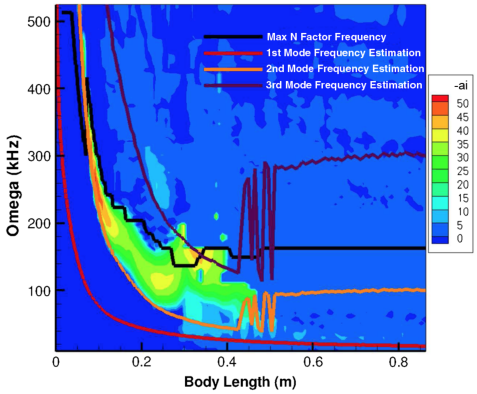

(b) LST results for centerline

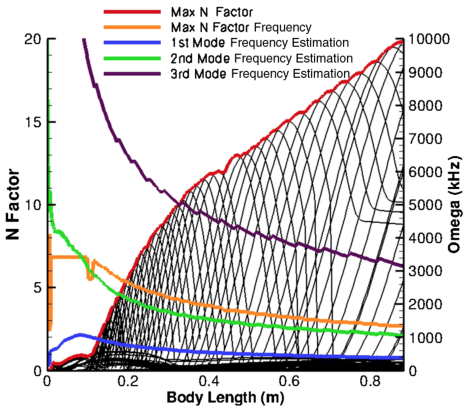

(c) PSE results for leading edge

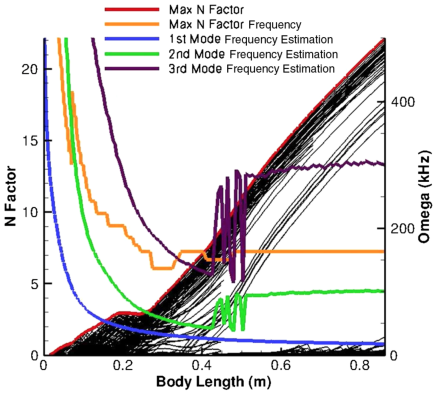

(d) PSE results for centerline

Figure 1.4: LST and PSE analysis for HIFiRE 5 21km case. [1]

It was concluded by Gosse *et al.* that although the geometry is a relatively simple configuration, the resulting three-dimensionality of the boundary layer provided a difficult flow configuration resulting in inaccurate/unreliable stability estimations in certain regions of the flow.

The difficulty of these classical methods to provide accurate/reliable estimations

motivates the development of more advanced tools to compliment the current methodologies. Space vehicles are inherently three-dimensional and possibly more complex than the configuration shown previously. With increasing computational power, advancements in large sparse linear solvers, and the current capabilities of unstructured parallel Navier-Stokes solvers, we can develop fully three-dimensional linear stability analysis tools that will provide accurate/reliable linear stability estimation for complex three-dimensional flows.

1.5 Overview of Dissertation

- Chapter 2 presents an overview and background into the basics of linear stability analysis for fluid systems. The Navier-Stokes equations for compressible flow are introduced. The Navier-Stokes equations are the mathematical basis for fluid dynamics, and are thus the basics of hydrodynamic stability. Modal analysis is first introduced. Assumptions and consequences of the approach are discussed. The overview of the several analysis procedures under the modal analysis approach is introduced and relevant literature is provided. The chapter is completed with a discussion of two solution methodologies that are prominent in literature, one of which is implemented in the code developed in this work.

- Chapter 3 the finite volume formulation is introduced. Formulation for inviscid and viscous spatial fluxes along with explicit and implicit time integration is covered. A brief discussion of the code used to obtain base flows, US3D, follows and relevant numerics are discussed. Next, Linear analysis of the Navier-Stokes operator is introduced. A method on how to obtain the linear operator from a non-linear base flow, known as matrix extraction, using parallel perturbation is introduced. Finally, the global modal analysis solver, GMUAS3D, developed to study three-dimensional complex flows is discussed.

- Chapter 4 presents the results to verify the computation tools. First, a subsonic cylinder case is introduced. This configuration is considered to be a canonical case for global stability analysis. The results generated by GMAUS3D and their comparison to literature are discussed. Next, a supersonic blunt cone is considered. This case enables a direct comparison of global methods against classical LST/PSE approaches. The chapter ends with a discussion of the implication of global methods and how they can be used as a predictive tool.

- Finally, Chapter 5 discusses the findings from Chapter 4. Conclusions about the performance of the codes developed are presented and future work is proposed.

Chapter 2

Modal Stability Analysis

Small amplitude disturbances, when superimposed onto a steady base state, can amplify or decay. The amplification of these disturbances can become significant such that they begin to interact with the underlying steady base state, resulting in augmentation or transition of the steady laminar boundary layer profile. Several mathematical techniques have been employed to characterize the behavior of small amplitude disturbances. One of the most widely used approaches relies on the assumption of "normal mode" behavior of the disturbances. The result of this assumption is an eigenvalue system which is solved to produce eigenvalues and eigenvectors. The measure of instability is determined by the sign and magnitude of the eigenvalue. This amplification/decay is assumed to have an exponential time dependence, resulting in what is classically known as Lyapunov stability. The associated eigenvector is then a shape of the disturbance.

This chapter presents an overview of the analysis techniques used to study boundary layer stability within a linear analysis context. The first section focuses on the linearization of the governing equations. Next, modal analysis is introduced with a discussion of the various assumptions and associated terminology common in literature. Finally, various solution methodologies are presented and discussed.

2.1 Linear Analysis

Linear analysis is concerned with the dynamics of small perturbations that are superimposed onto a steady or time periodic flow known as the base state. The amplitudes of the disturbance fluctuations are significantly small such that their behavior is governed by a linear equation. To derive the governing equation for small amplitude perturbations, we first start with an initial value problem that describes the nonlinear system,

$$\frac{\partial \mathbf{Q}}{\partial t} = \mathbf{M}\mathbf{Q}. \tag{2.1}$$

Here, $\mathbf{M}$ represents a nonlinear operator that acts on the vector of variables $\mathbf{Q}$. The operator $\mathbf{M}$ may represent any nonlinear global operator such as Burger's equation, the nonlinear wave equation, or the Navier-Stokes equations. In the case of the Navier-Stokes equations, dynamics of small perturbations that are superimposed upon a base flow will be governed by the Linearized Navier-Stokes Equations (LNSE). Linear stability analysis first starts with the decomposition of the vector $\mathbf{Q}$ into a basic state ($\mathbf{Q}_B$) plus a perturbation ($\mathbf{q}$),

$$\mathbf{Q}(\mathbf{x}, t) = \mathbf{Q}_B(\mathbf{x}) + \epsilon\, \mathbf{q}(\mathbf{x}, t). \tag{2.2}$$

The vector $\mathbf{x}$ represents the vector of space-coordinates (x, y, z), t is time, and $\epsilon << 1$ scales the perturbations to be much smaller than the base flow quantities. This ensures that products of $\mathbf{q}$ will be negligibly small, resulting in a linear system of equations for the dynamics of small amplitude perturbations. Substituting 2.2 into the nonlinear governing equation 2.1, subtracting off the base flow terms, and neglecting the nonlinear terms (order ϵ^2), results in an initial value problem for a disturbance $\mathbf{q}$,

$$\frac{\partial \mathbf{q}}{\partial t} = \mathcal{A}(\mathbf{Q}_B)\, \mathbf{q}. \tag{2.3}$$

The operator $\mathcal{A}(\mathbf{Q}_B)$ depends only on the base state $\mathbf{Q}_B$, while the vector $\mathbf{q}$ represents the vector of disturbances. Equation 2.3 may be considered a linear initial-boundary-value-problem (IBVP). From here, linear analysis requires a base state. With sufficient resolution, the analysis of stability can be obtained by running a set of initial conditions and tracking the energy amplification over time. Although a DNS resolution of the linear dynamics will give the most insight into individual disturbances, the feasibility of performing a computation for many initial conditions becomes cumbersome and computationally expensive. Assessment of the behavior of the global operator $\mathcal{A}$ can be extracted through modal analysis.

2.2 Governing Equations

The flow fields considered within this thesis are best described by thermally and calorically perfect air within the continuum regime. Specifically, the compressible Navier-Stokes equations best approximate the Mach numbers of which we are interested.

2.2.1 Compressible Navier-Stokes Equations

Below are the relevant conservation equations using standard summation convention.

Continuity

$$\frac{\partial \rho}{\partial t} + \frac{\partial}{\partial x_j}\left[\rho u_j\right] = 0. \tag{2.4}$$

Momentum

$$\frac{\partial \rho u_i}{\partial t} + \frac{\partial}{\partial x_j}\left[\rho u_i u_j\right] = -\frac{\partial p}{\partial x_i} + \frac{\partial}{\partial x_j}\left[\tau_{ij}\right]. \tag{2.5}$$

Energy

$$\frac{\partial E}{\partial t} + \frac{\partial}{\partial x_j}\left[(E+p)\,u_j\right] = -\frac{\partial q_i}{\partial x_i} + \frac{\partial}{\partial x_j}\left[u_i \tau_{ij}\right]. \tag{2.6}$$

In these equations ρ is the fluid density, ρu_i is the momentum in the i-th direction, and E is the total energy of the fluid. The variable p defines the pressure of the fluid. Using Stokes assumption ($\lambda = -\frac{2}{3}\mu$), the viscous stress, τ_{ij}, is defined as,

$$\tau_{ij} = \mu\left(\frac{\partial u_i}{\partial x_j} + \frac{\partial u_j}{\partial x_i} - \frac{2}{3}\frac{\partial u_k}{\partial x_k}\delta_{ij}\right) \tag{2.7}$$

where Sutherland's Law is used to define the viscosity.

$$\mu = \mu_{\text{ref}}\frac{T^{\frac{3}{2}}}{T+S}. \tag{2.8}$$

Here the constants are defined as $\mu_{\text{ref}} = 1.458\times10^{-6}$, and $S = 110.3$. Using Fourier's Law of heat conduction the heat transfer variable q, and is given as

$$q_i = -\kappa\frac{\partial T}{\partial x_i}, \tag{2.9}$$

where κ is related to the Prandtl number by $\text{Pr} = c_p\mu/\kappa$. For most conditions in air, the Prandtl number may be given as a constant of 0.72. Closure of the system of equations is given with an ideal gas assumption, $p = \rho RT$, where R is the specific gas constant.

2.2.2 Linearized Euler Equations

The previous section introduced the Navier-Stokes equations for a perfect gas. The behavior of small amplitude disturbances, which govern linear stability behavior, is obscured within the full non-linear Navier-Stokes equations. In order to extract the

governing equations, we must linearize the above set of equations. This is done by introducing Eq. 2.2 into the Navier-Stokes equations (Eq. 2.4 - 2.6, with associated constitutive relations). The result is a set of equations known as the Linearized Navier-Stokes Equations (LNSE). To show a simple example, we will linearize the Euler equations (inviscid Navier-Stokes equations) with respect to the variables (ρ, u, v, w, E). It is important to note that the choice of variables to linearize with respect to will have certain consequences in the implementation of boundary conditions and numerical switches.

Linearized Continuity

$$\frac{\partial \rho'}{\partial t} + \frac{\partial}{\partial x_j}\left[\rho' \bar{u}_j\right] + \frac{\partial}{\partial x_j}\left[\bar{\rho} u'_j\right] = 0. \tag{2.10}$$

Linearized Momentum

$$\frac{\partial \rho' \bar{u}_i + \bar{\rho} u'_i}{\partial t} + \frac{\partial}{\partial x_j}\left[\rho' \bar{u}_i \bar{u}_j + \bar{\rho} u'_i \bar{u}_j + \bar{\rho} \bar{u}_i u'_j\right] = -\frac{\partial p'}{\partial x_i}. \tag{2.11}$$

Linearized Energy

$$\frac{\partial e}{\partial t} + \frac{\partial}{\partial x_j}\left[(e+p)\,\bar{u}_j\,(E+P)\,u'_j\right] = 0. \tag{2.12}$$

We can write an explicit relation between the pressure and energy with the assumption of perfect gas by

$$P = (\gamma - 1)\left(E - \frac{1}{2}\rho\,(U_i U_i)\right).$$

The linearization of the equation then gives a closure to the above equations,

$$p' = (\gamma - 1)\left(e - \frac{1}{2}\rho\,(\bar{u}_i \bar{u}_i)) - \bar{\rho}\left(u'_i \bar{u}_i\right)\right).$$

2.3 Modal Analysis of the Navier-Stokes Equations

Modal analysis characterizes the behavior of disturbances using eigenvalue analysis. The scope of the derivations here will focus on the LNSE. The growth of a disturbance is determined when an eigenvalue crosses the complex half plane (from a negative value to positive). The derivation of modal analysis given in this chapter will follow a similar definition as given by Juniper *et al.* [30]. Starting from Eq. 2.3, we first make an assumption of the physical characteristics of the underlying base flow which will allow the exploitation of spatial invariances and reduce the size of the corresponding eigenvalue system to be solved. The vector $\mathbf{q}$ can be expressed in "normal mode" form,

$$\mathbf{q}\left(\mathbf{x},t\right)=\hat{\mathbf{q}}\left(\mathbf{x}^{*}\right)\exp\left[\Theta\left(\mathbf{x}^{*},t\right)\right]$$

The resulting transformation is called a modal assumption. The vector $\hat{\mathbf{q}}$ is called the shape function. This is the spatial shape of the disturbances that are resolved by the computational domain. The term in the exponential, Θ, is known as the phase function. The phase function assumes harmonic behavior of disturbances in directions for which the base flow is assumed to be spatially invariant and thus not resolved numerically. This is similar to a Fourier decomposition. The main point of this assumption is the separation of the space and time dependance of the disturbances. Depending on the character of the underlying base flow, the choice for Θ produces eigenvalue problems that vary in numerical accuracy as well as computational cost.

(A)	$\mathbf{q}(x,y,z,t) =$	$\hat{\mathbf{q}}(y)$	$e^{\imath(\alpha x+\beta z-\omega t)}$	LST	(Local)
(B)	$\mathbf{q}(x,y,z,t) =$	$\hat{\mathbf{q}}(\xi,y)$	$e^{\imath\left(\int \alpha(\xi)d\xi+\beta z-\omega t\right)}$	PSE	(Semi-Local)
(C)	$\mathbf{q}(x,y,z,t) =$	$\hat{\mathbf{q}}(y,z)$	$e^{\imath(\alpha x-\omega t)}$	BiGlobal	(Global)
(D)	$\mathbf{q}(x,y,z,t) =$	$\hat{\mathbf{q}}(\xi,y,z)$	$e^{\imath\left(\int \alpha(\xi)d\xi-\omega t\right)}$	PSE3D	(Global)
(E)	$\mathbf{q}(x,y,z,t) =$	$\hat{\mathbf{q}}(x,y,z)$	$e^{-\imath\omega t}$	TriGlobal	(Global)

Table 2.1: Hierarchy of the normal mode assumption. (A) local stability analysis (often referred to as simply LST analysis). (B) Parabolized Stability Equations in 2D. (C) BiGlobal Stability Analysis. (D) Parabolized Stability Equations in 3D. (E) TriGlobal Stability Analysis. NOTE: The choice of coordinate space directions (x, y, z) need not be exactly as stated here.

The progression from local to global analysis shown in Table 2.1 follows from the simplest form of linear analysis (A), to the most general form (E). Depending on the assumptions made for the underlying base flow, the stability analysis can be categorized as either 'local' or 'global' analysis approaches.

2.3.1 Local Approaches

The first two approaches shown in Table 2.1 are considered to be 'local' analysis approaches. The term local refers to the assumption of locally parallel or weakly non-parallel flow for the base flow quantities. These assumptions result in a restriction for the direction in which the disturbances are allowed to propagate. Spatially invariant directions are then represented by spatial wave numbers.

Local Stability Analysis

The top level in Table 2.1, represents the most drastic assumptions of the underlying base flow. This approach is considered to be the most common approach and was popularized by Mack [31]. Here the base flow is assumed to be spatially invariant in two coordinate directions. The assumption here is that the dynamics of the disturbance in the two spatially invariant directions may be assumed to be periodic and described by wave numbers, while in the third spatial direction, a computational mesh is used to fully resolve the spatial structure. This approach is known as Linear Stability Theory and is often referred to in literature as LST. The advantage of this method is the reduction of the spatial behavior of the disturbance to a single coordinate direction, which in turn results in large computational savings. Application of LST has been successfully applied to flows which exhibit locally parallel behavior such as channel flows, and shear layers.

However, the assumptions that go along with this type of analysis can become invalid. In the case of fast growing boundary layers, separated/re-circulatory flow, or base flows which exhibit strong three-dimensionality.

Parabolized Stability Equations

To account for the case of one weakly varying spatial direction as is seen for boundary/shear layers, the introduction of "semi-local" analysis (method B) provides a more appropriate representation. By augmenting the Navier-Stokes equations through the assumptions of downstream propagating waves, a set of equations are introduced known as the parabolized stability equations. Similar to LST, these equations consist of a fast oscillatory part and a shape function that varies slowly in the streamwise direction. This decomposition results in a system that is parabolic in the streamwise direction which is amenable to marching solutions. For a detailed explanation of the underlying mathematical approach, the reader is referred to the work of Herbert *et al* [32].

The application of the parabolized stability equations has provided computationally efficient results for boundary stability estimation. The work of Balakumar *et al.* [2] show good agreement with DNS results.

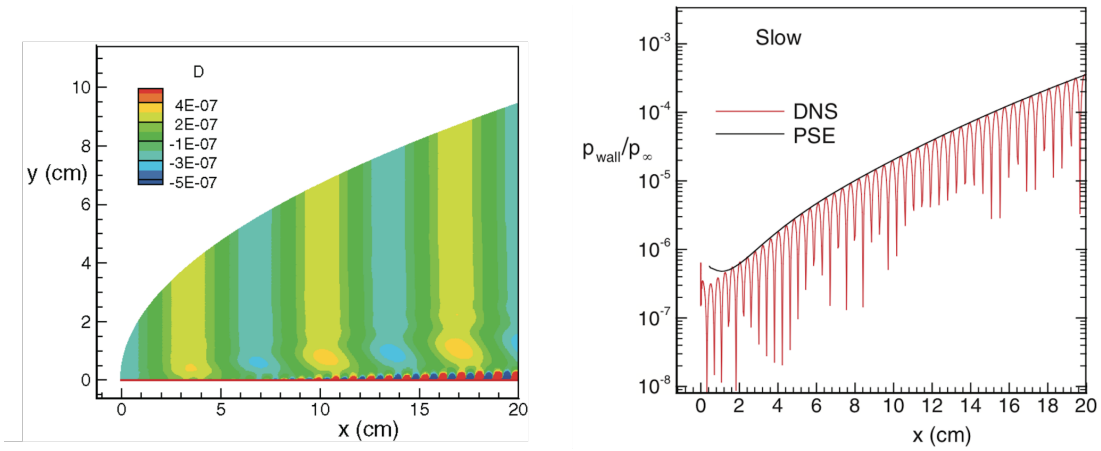

(a) DNS Results

(b) Comparisons between DNS and PSE

Figure 2.1: PSE analysis compared to DNS results for a flat plate boundary layer. (Balakumar *et al.*[2])

2.3.2 Global Approaches

Approaches (C)-(D) are considered global approaches. The term global refers to at least two spatial directions in which the disturbance is computationally resolved. Depending on which approach is considered, the final spatial direction can be assumed spatially invariant, slowly varying, or can be fully resolved. These global approaches are referred to as BiGlobal, PSE3D, and TriGlobal analysis, respectively. An brief overview of the global approaches is described below.

BiGlobal

The first of the global approaches is known as BiGlobal stability. The term BiGlobal refers to the shape function being dependent on two spatial directions. This results in a plane for which the disturbance must be computationally resolved. The disturbances are able to propagate in two dimensions (characteristics allowing), while the third dimension is prescribed a wave number. This approach has been successfully implemented for a range of flows.

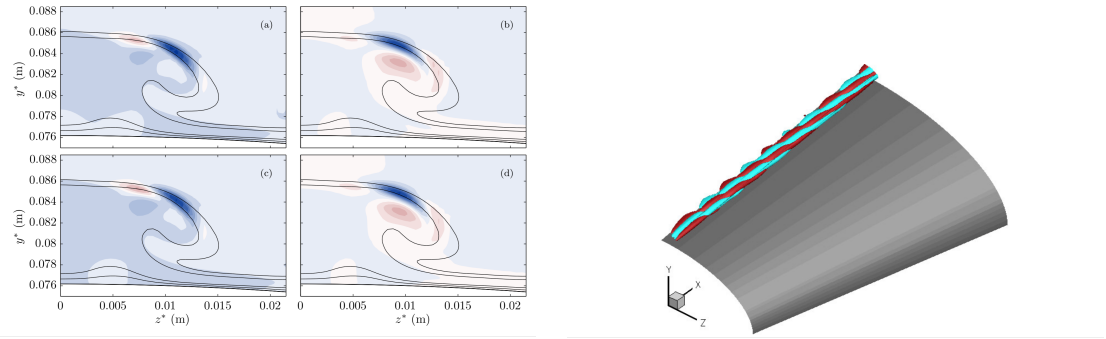

(a) BiGlobal planes

(b) Three-dimensional reconstruction of unstable mode

Figure 2.2: BiGlobal stability analysis performed by Theofilis *et al.* for HIFiRE 5 [3]

PSE3D

Similar to the extension from LST to PSE, PSE3D extends the BiGlobal approach to contain a weakly varying spatial direction normal to the BiGlobal plane. This allows marching solutions of entire BiGlobal planes in the downstream direction, which allows for a coupling of convecting disturbance quantities. While this method allows coupling of disturbances in the two-dimensional plane, the marching methodology restricts the disturbances to only be coupled in the downstream direction (i.e., preventing any

upstream traveling waves).

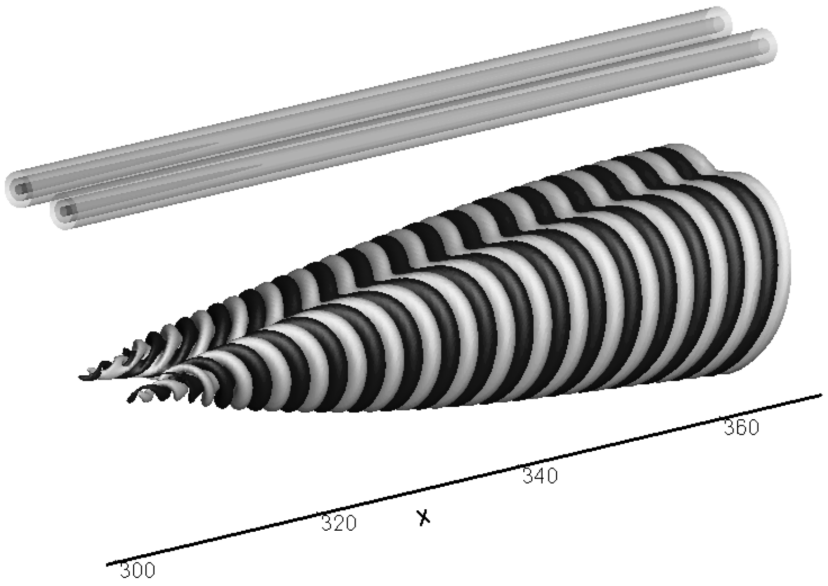

Figure 10. *Upper:* **Basic flow axial velocity and** *Lower*: **iso-surfaces** ($u/|u_0| = 100$ **and** $u/u_0| = -100$) **of axial velocity amplitude function in the range** $x \in [300, 370]$

Figure 2.3: PSE3D stability analysis performed by Theofilis *et al.*[4] for counter rotating vortex pair

TriGlobal

The most general approach to modal analysis is known as TriGlobal analysis. TriGlobal analysis makes no assumption of spatial invariance for the underlying base flow. Instead, the shape functions are fully resolved by the computational mesh. The resulting eigenvalues describe only the long-time dependence of the disturbances (i.e. amplification or decay) as well as oscillations (frequencies).

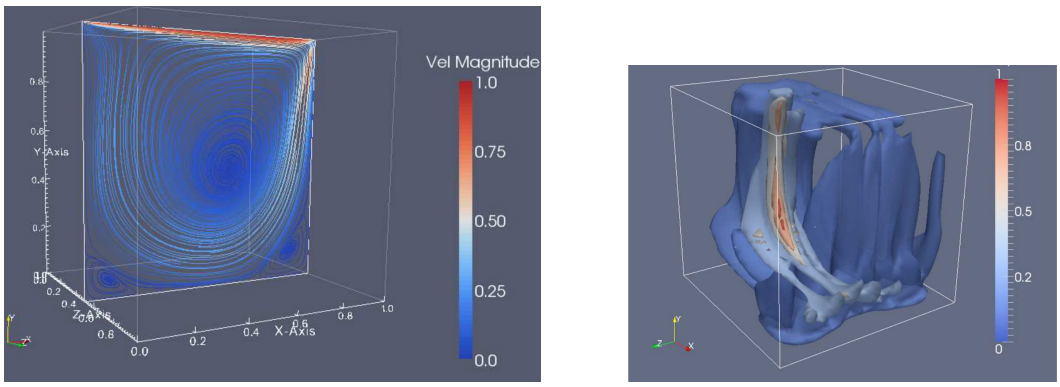

(a) Base flow

(b) Three-dimensional unstable mode

Figure 2.4: TriGlobal analysis performed by Gianneti *et al.* [5]

2.4 Solution Methodology

2.4.1 QR Decomposition

The most widely used method for computing eigenvalues is the QR algorithm [33]. The name of the algorithm comes from the use of an orthogonal matrix 'Q' and a triangular matrix 'R'. While the QR method will work, the convergence can be slow. Instead we will outline the algorithm which depends on the shifted QR method. The QR method itself is the second part of a two-step process. Given a standard eigenvalue problem defined by,

$$\lambda \mathbf{x} = \mathbf{A}\mathbf{x}, \tag{2.13}$$

where $\mathbf{A} \in \mathbb{C}^{n \times n}$. The first step is to bring the matrix $\mathbf{A}$ into upper Hessenberg form (i.e. a matrix with zeros below the first subdiagonal). Introducing a unitary matrix $\mathbf{V}$

and a Hessenberg matrix $\mathbf{H}$,

$$\mathbf{AV} = \mathbf{VH}, \tag{2.14}$$

where $\mathbf{V} \in \mathbb{C}^{n\times n}$ and $\mathbf{H} \in \mathbb{C}^{n\times n}$. This can be done using a Householder technique. The second step is to iteratively apply QR decompositions on $\mathbf{H}$ to reduce the lower diagonal elements to zero. The result is then a system that is converged to Schur form,

$$\mathbf{AQ} = \mathbf{QU}. \tag{2.15}$$

The matrix $\mathbf{A}$ is thus decomposed into a unitary matrix $\mathbf{Q}$ and an upper Hessenberg matrix $\mathbf{U}$. The diagonal entries of $\mathbf{U}$ contain the eigenvalues of $\mathbf{A}$.

While this method results in the exact extraction of the eigenvalues of the operator $\mathbf{A}$, the cost of the Q-R decomposition can be prohibitively expensive to perform. The total work required for the standard Q-R decomposition is $\mathcal{O}(n^3)$ flops. For large problems (matrices exceeding dimensions $n \approx 10^5$), direct methods cannot be applied and one must resort to iterative techniques.

2.4.2 Arnoldi Method

Alternative to the direct method of QR, one may employ an iterative technique such as the Krylov based approach known as the Arnoldi Method [34]. The Arnoldi method is considered an iterative technique and can be thought of as a truncated or partial reduction of matrix $\mathbf{A}$ to Hessenberg form. This method makes use of the stabilized Gram-Schmidt procedure for a small subset of m vectors, where $m << n$ for a matrix $\mathbf{A} \in \mathbb{C}^{n\times n}$

$$\mathbf{AV}_m = \mathbf{V}_m\mathbf{H}_m + \mathbf{r}_m e_m^T \tag{2.16}$$

Again, our global operator is sill $\mathbf{A} \in \mathbb{C}^{n\times n}$, while now we express the m-dimensional orthonormal basis $\mathbf{V}_m = [\mathbf{v}_1, \mathbf{v}_2, ..., \mathbf{v}_m]$ as $\mathbf{V}_m \in \mathbb{C}^{n\times m}$. The upper Hessenberg matrix is also truncated $\mathbf{H}_m \in \mathbb{C}^{m\times m}$. The terms on the right represent the residual vector, $\mathbf{r}_m \in \mathbb{C}^{m\times 1}$, and the unit vector e_m^T.

Algorithm 1 The m-step Arnoldi Iteration

1: Let $\mathbf{A} \in \mathbb{F}^{n\times n}$.

2: $\mathbf{q}_1 = \mathbf{x}/\|\mathbf{x}\|$;

3: $\mathbf{z} = \mathbf{A}\mathbf{q}_1$ (Provided by the user);

4: $\alpha_1 = \mathbf{q}_1^*\mathbf{z}$;

5: $\mathbf{r}_1 = \mathbf{w} - \alpha_1\mathbf{q}_1$;

6: $Q_1 = [\mathbf{q}_1]$;

7: $H_1 = [\alpha_1]$

8: **for** $j = 1, ..., m-1$ **do**

9: $\beta_j := \|\mathbf{r}_j\|$; $\mathbf{q}_{j+1} = \mathbf{r}_j/\beta_j$;

10: $Q_{j+1} := [Q_j, \mathbf{q}_{j+1}]$; $\hat{H}_j := \begin{bmatrix} H_j \\ \beta_j \mathbf{e}_j^T \end{bmatrix} \in \mathbb{F}^{(j+1)\times j}$;

11: $\mathbf{z} = \mathbf{A}\mathbf{q}_j$ (Provided by the user);

12: $\mathbf{h} := Q_{j+1}^*\mathbf{z}$; $\mathbf{r}_{j+1} := \mathbf{z} - Q_{j+1}\mathbf{h}$;

13: $H_{J+1} := \left[\hat{H}_j, \mathbf{h}\right]$

14: **end for**

Chapter 3

Numerical Methods

3.1 The Finite Volume Method

We first begin with Eqs. 2.4-2.6 equations in vector form. Let U be the vector of conserved variables and the convective, $(\cdot)_c$, and viscous, $(\cdot)_v$, flux vectors be; F_c, G_c, H_c, F_v, G_v, H_v. The vector form of the governing equations becomes

$$\frac{\partial U_i}{\partial t} + \frac{\partial F_c}{\partial x} + \frac{\partial G_c}{\partial y} + \frac{\partial H_c}{\partial z} = \frac{\partial F_v}{\partial x} + \frac{\partial G_v}{\partial y} + \frac{\partial H_v}{\partial z}, \tag{3.1}$$

where the vectors are defined as

$$U = \begin{pmatrix} \rho \\ \rho u \\ \rho v \\ \rho w \\ \rho E \end{pmatrix},$$

$$F_c = \begin{pmatrix} \rho u \\ \rho uu + p \\ \rho uv \\ \rho uw \\ (\rho E + p)\, u \end{pmatrix}, \qquad G_c = \begin{pmatrix} \rho v \\ \rho vu \\ \rho vv + p \\ \rho vw \\ (\rho E + p)\, v \end{pmatrix}, \qquad H_c = \begin{pmatrix} \rho w \\ \rho wu \\ \rho wv \\ \rho ww + p \\ (\rho E + p)\, w \end{pmatrix}$$

$$F_v = \begin{pmatrix} 0 \\ \tau_{xx} \\ \tau_{xy} \\ \tau_{xz} \\ u\tau_{xx} + v\tau_{xy} + w\tau_{xz} - q_x \end{pmatrix}, \qquad G_v = \begin{pmatrix} 0 \\ \tau_{yx} \\ \tau_{yy} \\ \tau_{yz} \\ u\tau_{yx} + v\tau_{yy} + w\tau_{yz} - q_y \end{pmatrix},$$

$$H_v = \begin{pmatrix} 0 \\ \tau_{zx} \\ \tau_{zy} \\ \tau_{zz} \\ u\tau_{zx} + v\tau_{zy} + w\tau_{zz} - q_z \end{pmatrix}.$$

Combining the terms into a single vector function $F(U)$ as

$$\vec{F}(U) = (F_c - F_v)\vec{i} + (G_c - G_v)\vec{j} + (H_c - H_v)\vec{k}, \tag{3.2}$$

we can rewrite Eq. 3.1 in a more compact form:

$$\frac{\partial U_i}{\partial t} + \nabla \cdot \vec{F}(U) = 0. \tag{3.3}$$

The finite volume method discretizes space into small control volumes. The change

in the solution vector U is then described by fluxes across the surface of the control volume. To derive the finite volume form used in US3D, we first start by taking Eq. 3.3 and integrating over an arbitrary control volume. The resulting expression is known as an integral form.

$$\int_V \frac{\partial U_i}{\partial t} dV + \int_V \frac{\partial \vec{F}_i}{\partial x_j} dV = 0 \tag{3.4}$$

The integral containing the vector of conserved variables U represents the conserved variables within a control volume. The integral can instead be rewritten as simply the volume average of the conserved quantities $U \rightarrow \bar{U}$. Whereas flux $\vec{F}$ term is responsible for changes within the volume. Applying the divergence theorem to this term results in a change from a volume integral into a surface integral.

$$V_i \frac{\partial \bar{U}_i}{\partial t} + \oint_S \vec{F}_i \cdot d\vec{S} = 0 \tag{3.5}$$

Here, V_i represents the volume of cell i. Eq. 3.5 now connects internal changes to the conserved variables U to fluxes across its surface. Discretizing this equation can be achieved by changing the continuous surface integral across the volume bounding surface, into a sum of fluxes across discrete faces. Dropping the over-bar, and applying the volume dependence to the flux term, we get,

$$\frac{\partial \bar{U}_i}{\partial t} + \frac{1}{V_i} \sum_{faces} \left(\vec{F}_i \cdot \vec{n} \right) \vec{S} = 0 \tag{3.6}$$

where, $S = sx' + sy' + sz'$ is the normal for each face.

Eq. 3.6 is the discretized finite volume form and can be used to solve the Navier-Stokes equations for arbitrary flow domains that are discretized by discrete elements. The conserved quantities are stored at the cell centers, whereas the fluxes are computed across the faces of an fluid element. Note that the discretizing step does not denote a specific type of volumetric element. This means the equations are valid for various types of computational elements (i.e. hexahedral, tetrahedral, prisms, or combinations therein).

3.2 Spatial Fluxes

Spatial Integration is named such because we are extrapolating data stored at the cell centroid ($\bar{U}_i$), to the cell faces. While there are many spatial integration schemes available within the finite-volume framework, we will be focusing on the methods used to generate the base states presented. When evaluating the spatial portion of Eq. 3.6, the treatment of the viscous and inviscid contributions are handled differently. We will decompose the flux vector F_i into the inviscid convective flux, F_c, and a viscous diffusion flux, F_v.

$$\vec{F}_i = \vec{F}_c + \vec{F}_v \tag{3.7}$$

3.2.1 Inviscid Fluxes

The inviscid portion of the flux describes convection of fluid in and out of an element. When the fluid is supersonic, the inviscid portion of the flux is considered hyperbolic in nature (information travels along characteristics). The method of characteristics has been a powerful tool to to solving hyperbolic sets of equations in two dimensions. In the mid-1970s (corresponding to the rapid increase in computing power), characteristic theory became the basis for many algorithms such as Moretti's "Lambda" [35], Roe's flux difference vector splitting [36], and Steger-Warming flux splitting methods [37].

3.2.2 Steger-Warming Flux Vector Splitting

Steger and Warming performed flux vector splitting based on characteristic theory in conservation law form. Steger and Warming discovered that the flux vector for the Euler equations are homogeneous with respect to the vector of conserved quantities. In terms of the flux vector F_c this means the flux vector can be rewritten exactly using a Jacobian,

$$F = \frac{\partial F}{\partial U} U = AU$$

Here, A represents the Jacobian. Since we are dealing with a characteristic based method, it is convenient to express the Jacobian in the form of primitive variables. We first introduce a vector of primitive variables $V = (\rho, u, v, w, T)$. From here we can rewrite the Jacobian matrix A as,

$$A = \frac{\partial F}{\partial U} = \frac{\partial F}{\partial V} \frac{\partial V}{\partial U}$$

Next, we introduce the Jacobians representing transformations from conservatives to primitives, $\frac{\partial U}{\partial V}$, and primitives and conservatives, $\frac{\partial V}{\partial U}$. Noting the product $\frac{\partial U}{\partial V} \frac{\partial V}{\partial U} = I$, we can premultiply the above expression by unity to get;

$$A = \frac{\partial F}{\partial U} = \frac{\partial U}{\partial V}\frac{\partial V}{\partial U}\frac{\partial F}{\partial V}\frac{\partial V}{\partial U}$$

We will represent the transformation matrix to and from primitive space as $S = \frac{\partial V}{\partial U}$ and $S^{-1} = \frac{\partial U}{\partial V}$, and the central portion as the Matrix M.

$$A = S^{-1}MS$$

This is known as a similarity transformation. The similarity matrix, $M = \frac{\partial V}{\partial U}\frac{\partial F}{\partial V}$, shares the same eigenvalues as A. The final step before splitting is diagonalizing the matrix M to find its eigenvalues Λ;

$$M = C^{-1}\Lambda C$$

Here, C is the matrix containing columns of eigenvectors associated to the diagonal matrix Λ of eigenvalues. For the Euler equations, the eigenvalues will only have 3 unique values; u', $u' + c$, $u' - c$, where $u' = u \cdot sx' + v \cdot sy' + w \cdot sz'$ is the velocity component normal to the face and c is the speed of sound. Rewriting the inviscid flux now as,

$$F_c = AU = \left(\frac{\partial U}{\partial V}C^{-1}\Lambda C\frac{\partial V}{\partial U}\right)U$$

We can now performing the splitting of the inviscid flux into "left" (positive) and "right" (negative) moving components based on the sign of the eigenvalues in Λ.

$$F_c = F^+ + F^-$$
$$F^+ = \left(\frac{\partial U}{\partial V}C^{-1}\Lambda_+ C\frac{\partial V}{\partial U}\right)U_i$$
$$F^- = \left(\frac{\partial U}{\partial V}C^{-1}\Lambda_- C\frac{\partial V}{\partial U}\right)U_{ii}$$

F_c^+ and F_c^- represent the upwinded inviscid flux running parallel and antiparallel to the face normal, respectively. To first-order, the Steger-Warming method for the inviscid flux is solved numerically by;

$$F^+_{i+\frac{1}{2}} = A_i^+ U_i$$
$$F^-_{i+\frac{1}{2}} = A_{ii}^- U_{ii}$$

Where A_i^+ and A_{ii}^- are evaluated using the values from the left and right cells of face $i + \frac{1}{2}$, respectively. This method, while robust, produces a significant amount of numerical dissipation. An improvement to this method is available through the Modified Steger Warming approach and produces less dissipation. The formulation is very similar but with the difference being the values in the Jacobian are evaluated from the face average;

$$F^+_{i+\frac{1}{2}} = A^+_{i+\frac{1}{2}} U_i \quad \text{and} \quad F^-_{i+\frac{1}{2}} = A^-_{i+\frac{1}{2}} U_{ii} \tag{3.8}$$

High Order Upwind Flux Schemes

The previous section derived the first order Steger-Warming and Modified Steger-Warming methods. To achieve high-order, more accurate extrapolations of variables to the face can be done. This is done by representing the left and right states of the face $i+\frac{1}{2}$ using a function dependent on a number of cells. For a structured one dimensional grid, this would look something like,

$$U_L = f\left(U_i, U_{i-1}, ...\right)$$

$$U_R = f\left(U_i, U_{i+1}, ...\right)$$

Replacing the variables U_i and U_{ii} in Eq. 3.8 with U_L and U_R,

$$F^+_{i+\frac{1}{2}} = A^+_{i+\frac{1}{2}} U_L \quad \text{and} \quad F^-_{i+\frac{1}{2}} = A^-_{i+\frac{1}{2}} U_R \tag{3.9}$$

Results in the more general form of the Modified Steger-Warming flux scheme. High-order MUSCL reconstruction of U_L and U_R is often used. Alternatively, one can use gradient-based reconstruction methods which provide an advantage on unstructured meshes. Higher-order flux methods provide higher resolution around discontinuities, but also are susceptible to spurious oscillations near such points. It is advisable to invoke flux limiters to switch between the more dissipative (and stable) first order upwind schemes near strong discontinuities, and high-order (high resolution) schemes in regions of importance.

Flux Limiters

Flux limiters provide a means to switch between high-resolution flux reconstruction schemes such as the popular MUSCL extrapolation, and stable first-order upwind schemes, to avoid spurious oscillations, thus "limiting" the spatial derivatives to physically realizable and meaningful values. Representing high-resolution fluxes as H and low resolution fluxes as L, a general flux limiter is implemented as

$$F_{i+\frac{1}{2}} = L_{i+\frac{1}{2}} - \phi\left(r_i\right)\left(L_{i+\frac{1}{2}} - H_{i+\frac{1}{2}}\right), \tag{3.10}$$

where the limiter ϕ is a function of the smoothness parameter r_i. The smoothness parameter is a measure of the local rate of change in the gradient, and is evaluated as

$$r_i = \frac{U_i - U_{i-1}}{U_{i+1} - U_i}.$$

The flux limiter function is constrained to be $\phi(r_i) \geq 0$. When $\phi = 0$, strong gradients are present in the flow and Eq. 3.10 reverts to the stable low-resolution flux schemes. Alternatively, when $\phi = 1$, the solution gradients are smooth and a high-resolution flux can be recovered. There are many ways to define the limiter function ϕ and its switching characteristics, with no one limiter proving to work well for all problems. Examples of some popular limiters are;

$$\begin{aligned} \phi(r) &= \max[0, \min(1, r)] && \text{Min-Mod (symmetric) [36]} \\ \phi(r) &= \max[0, \min(2r, 1), \min(r, 2)] && \text{Superbee (symmetric)[36]} \\ \phi(r) &= \frac{r + |r|}{1 + |r|} && \text{Van-Leer (symmetric) [38]} \end{aligned} \tag{3.11}$$

The way in which these limiters switch between low and high-resolution schemes differ. The Min-mod limiter is considered to be the most conservative in switching, while the Superbee is the most aggressive, and Van-Leer represents a smooth function somewhere between the two. The importance of their differences will be highlighted in a later section when discussing their effect on the evaluation of the numerical Jacobian in relation to stability analysis. All of the above examples are considered symmetric. Mathematically this means $\frac{\phi(r)}{r} = \phi\left(\frac{1}{r}\right)$. Specifically, this means the limiter function behaves the same for gradients in both directions. A desirable feature of the above limiters is that they are all second order Total Variation Diminishing (TVD). In order for a limiter to be TVD, Sweby [6] showed that it must pass through the shaded region displayed in Figure 3.1. It becomes clear that all formulations of limiter functions must pass through the $\phi(1) = 1$ point and lie within the shaded region to be considered

second order TVD.

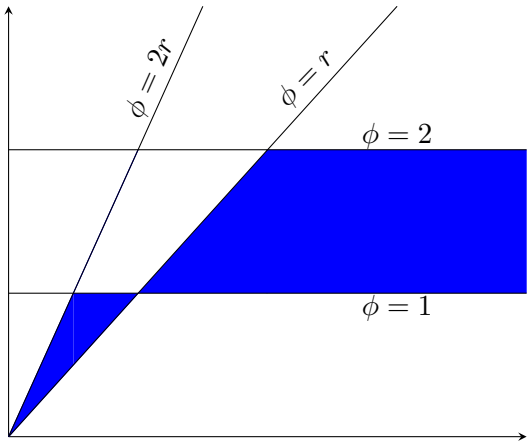

Figure 3.1: Admissible limiter region for second-order TVD Sweby [6]

Central Schemes

The previous section introduced the concept of flux limiting to allow high and low-resolution upwind fluxes to be applied to flows with strong gradients. Flux limiting allows high-resolution upwind fluxes to be used in smooth regions of the flow to increase accuracy, and low-resolution upwinded fluxes where stability is required. For both high and low-resolution upwinded flux schemes, the amount of dissipation is higher than a corresponding central scheme of the same order. The increased amount of numerical dissipation requires higher mesh resolution in order to capture important flow physics. To counter this, we look to augment the fluxes presented in Eq. 3.8. Taking the total flux to be $F = F^+ + F^-$ and expanding the Jacobian matrices A^+ and A^-, we first write;

$$F = \left(\frac{\partial U}{\partial V} C^{-1} \Lambda_+ C \frac{\partial V}{\partial U}\right) U_i + \left(\frac{\partial U}{\partial V} C^{-1} \Lambda_- C \frac{\partial V}{\partial U}\right) U_{ii} \tag{3.12}$$

We can manipulate the above expression as;

$$
\begin{aligned}
F &= \left(\frac{\partial U}{\partial V} C^{-1} \Lambda_{+} C \frac{\partial V}{\partial U}\right) U_i + \left(\frac{\partial U}{\partial V} C^{-1} \Lambda_{-} C \frac{\partial V}{\partial U}\right) U_{ii} \\
&= \left(\frac{\partial U}{\partial V} C^{-1} \frac{\Lambda_{+} + |\Lambda|}{2} C \frac{\partial V}{\partial U}\right) U_i + \left(\frac{\partial U}{\partial V} C^{-1} \frac{\Lambda_{-} + |\Lambda|}{2} C \frac{\partial V}{\partial U}\right) U_{ii} \\
&= \left(\frac{\partial U}{\partial V} C^{-1} \Lambda C \frac{\partial V}{\partial U}\right) \frac{U_i + U_{ii}}{2} + \left(\frac{\partial U}{\partial V} C^{-1} |\Lambda| C \frac{\partial V}{\partial U}\right) \frac{U_i - U_{ii}}{2} \\
&= A \frac{U_i + U_{ii}}{2} + |A| \frac{U_i - U_{ii}}{2}
\end{aligned}
$$

Similar to the previous section, we now have a flux that is split into a stable but dissipative upwind portion, $F_{dissipative} = |A| \frac{U_i - U_{ii}}{2}$, and a symmetric lower-dissipation central part, $F_{symmetric} = A \frac{U_i + U_{ii}}{2}$. Both terms may be evaluated separately and added together with the upwinded portion being modulated by a function α, such that it is only active in regions where additional dissipation is needed for stability,

$$F = F_{symmetric} + \alpha \cdot F_{dissipative}.$$

Here, α is a function that is equal to 1 in regions where dissipation is needed (such as strong shocks), and equal to 0 in regions where no dissipation is required.

3.2.3 Viscous Fluxes

The viscous portion of the fluxes rely on gradient information at each face. There are a few ways to compute the gradients at the face. One way would involve storing the local, unique, stencil for each face and compute the gradients using this stencil at each time-step. This would be the most accurate, but also the most expensive both in terms of computational-efficiency and memory overhead. Another way is to leverage the cell-centered gradients that are used for high-order inviscid methods. These gradients are then reconstructed to face-centered gradients.

There are many ways to perform gradient reconstruction. Methods such as Green-Gauss provide an inexpensive way to reconstruct the gradients but are prone to errors

[39, 40]. Another approach is using Weighted-Least-Squares. This approach solves for the gradient reconstruction by minimizing the sum of the squares of the differences between stencil neighbor values and the values extrapolated from the cell of interest to said neighboring values. A final example of face gradient reconstruction is known as the deferred correction approach [41] which provides face-centered gradients. This approach uses the average of the left and right cell gradients in the face normal and face parallel directions.

3.3 Temporal Integration

Time integration of the governing equations can either be performed in an explicit or implicit formulation. Explicit time integration limits the time step such that it obeys the Courant Friedrichs Lewy (CFL) condition to be less than 1. In practical terms, this means information may not travel faster than characteristic time for a perturbation to travel from one cell to an adjacent cell. Implicit time integration allows for much larger time steps, $CFL >> 1$. Implementation of explicit and implicit schemes have their own advantages and disadvantages.

3.3.1 Explicit

We first start with the governing Eq. 3.6,

$$\frac{\partial \bar{U}_i}{\partial t} + \frac{1}{V_i} \sum_{faces} \left(\vec{F}_i \cdot \vec{n} \right) \vec{S} = 0.$$

the time derivative may be evaluated to first order as,

$$\frac{\partial \bar{U}}{\partial t} = \frac{\bar{U}^{n+1} - \bar{U}^n}{\triangle t}.$$

where n represents the current time and $n+1$ is the future time.

Implementing this expression into the above equation results in the most simple and cheapest (per iteration) explicit scheme is known as the explicit Euler scheme.

$$\bar{U}^{n+1} = \bar{U}^n - \frac{\triangle t}{V_i} \sum_{faces} \left(\vec{F}_i^n \cdot \vec{n} \right) \vec{S} = \bar{U}^n + \delta \bar{U} \tag{3.13}$$

where $\delta \bar{U}$ represents the residual (change) to the conserved variables.

For higher-order approximations, one can extend Eq. 3.13 to have several sub-iterations. A popular method which uses this approach is the Runge-Kutta schemes. These schemes are more expensive as they require several residual evaluations per time step.

3.3.2 Implicit

Implicit time integration allows for larger time steps to be taken. This is advantageous on computational meshes with large ranges in cell size (such as meshes with clustering near walls to resolve viscous gradients). The large time step comes at the cost of solving a linear system of equations. The explicit formulation from the previous section can be made implicit simply by evaluating the fluxes at the $n+1$ time step.

$$\bar{U}^{n+1} = \bar{U}^n - \frac{\triangle t}{V_i} \sum_{faces} \left(\vec{F}_i^{n+1} \cdot \vec{n} \right) \vec{S} \tag{3.14}$$

We must now find a way to evaluate $\vec{F}_i^{n+1}$. This will require the inviscid and viscous parts to again be treated in a separate manner.

Inviscid Terms

Starting with the flux vector at the future time level, $n+1$, we will perform a Taylor series expansion about a small time perturbation $\triangle t$,

$$\begin{aligned}\vec{F}_i^{n+1} &= \vec{F}_i^n + \frac{\partial \vec{F}_i^n}{\partial U_i}\left(\bar{U}_i^{n+1} - \bar{U}_i^n\right) + \mathcal{O}\left(\triangle t\right) \\ &= \vec{F}_i^n + A_i^n \delta\bar{U}_i + \mathcal{O}\left(\triangle t\right)\end{aligned}$$

It is important to note here that the linearized split flux uses the same split Jacobians A as was seen in Eq. 3.9. This means we can write the flux at face $i+\frac{1}{2}$ as,

$$\vec{F}^{+n+1}_{i+\frac{1}{2}} = A^n_{+,i+\frac{1}{2}} U_i^{n+1} + A^n_{-,i+\frac{1}{2}} U_{ii}^{n+1} + A^n_{+,i+\frac{1}{2}} \delta U_i + A^n_{-,i+\frac{1}{2}} \delta U_{ii}$$

replacing Eq. 3.14 with the above expression and rearrange results in a general form of the implicit system for the inviscid part of the flow,

$$\delta\bar{U} + \frac{\triangle t}{V_i} \sum_{faces} \left(A^n_{+,f}\delta U_i + A^n_{-,f}\delta U_{ii}\right)\cdot \vec{n}_f \;\; \vec{S}_f = -\frac{\triangle t}{V_i} \sum_{faces} \left(F_f^n \cdot \vec{n}_f\right) \vec{S}_f \tag{3.15}$$

δU is now the implicit update to the conserved variables with i representing the current cell, and ii the corresponding cell neighbor at face f.

Viscous Terms

Linearization of the viscous fluxes about the state vector is needed to complete the implicit form of the equation set. As mentioned in the previous viscous spatial fluxes section, explicit storage of the stencil is not computationally efficient. Instead the viscous fluxes are computed using one of several different gradient reconstruction methods. Because of this, the viscous Jacobians are not computed and stored, a fact that will become important later in the numerical Jacobian. To remedy this, we take an

approximate form of the viscous Jacobians, M, and assume derivatives that are not in the face-normal direction can be neglected. We then rewrite the fluxes as,

$$F_v = M\frac{\partial}{\partial \eta}V$$

Where η represents the face-normal direction, and V is the vector of primitive variables. A change of variables is introduced to map back to the conservative set U resulting in,

$$F_v = M\frac{\partial}{\partial \eta}\left(\frac{\partial V}{\partial U}\delta U\right).$$

The above equation may now be evaluated at the $n+1$ time level creating an implicit system for the viscous contributions. Adding the viscous portion to Eq. 3.15, the final form of the general implicit set of equations is expressed as,

$$\delta\bar{U}+\frac{\triangle t}{V_i}\sum_{faces}\left(A^n_{+,f}\delta U_i + A^n_{-,f}\delta U_{ii} + M\frac{\partial}{\partial\eta}N\left(\delta U_i - \delta U_{ii}\right)\right)\cdot\vec{n}_f \;\; \vec{S}_f = -\frac{\triangle t}{V_i}\sum_{faces}\left(F^n_f\cdot\vec{n}_f\right)\vec{S}_f \tag{3.16}$$

where N represents the Jacobian matrix $\frac{\partial V}{\partial U}$. Eq. is now the fully implicit set of the Navier-Stokes equations. With the addition of a linear solver, and appropriate treatment of the boundary conditions, the system may be iterated in time with global time-steps that exceed CFL= 1. Depending on the spatial stencil choice, the resulting linear operator is often large and sparse allowing for a range of linear solvers to be implemented for fast and efficient solutions.

3.4 US3D Flow Solver

The solver used to obtain base flows of interest is a three-dimensional unstructured finite volume Navier-Stokes solver, US3D, that was developed at the University of Minnesota [42]. The unstructured implementation allows for a wide variety of complex mesh

topologies to be used to leverage local refinement and complex geometry simulations.

Spatial integration is computed using either the second or third-order upwind, modified Steger-Warming (MacCormack and Candler [43]), or low-dissipation kinetic energy consistent (KEC) method developed by Subbareddy *et al* [44] flux scheme for the inviscid convective portion. Viscous fluxes are formed using a central, second-order accurate method.

Time integration methods within US3D allow for explicit and implicit solutions. Explicit temporal integration is available through the first-order Explicit Euler scheme. Higher order explicit schemes are available in the form of Runge-Kutta schemes and are up to third-order TVD accurate. Implicit integration is available in either first or second-order accurate Backwards Difference Formulation (BDF). First and second-order accurate Crank-Nicholson type scheme is also available.

3.5 STABL software suite

When assessing local and non-local stability, the Stability and Transition Analysis for hypersonic Boundary Layers (STABL) tool provides an efficient, parallel LST and PSE solver. Developed at the University of Minnesota by Heath Johnson, STABL is a software suite containing grid-generation, 2-D axisymmetric Navier-Stokes solver based on Data-Parallel Line Relaxation (DPLR) method [45], mean-flow analysis tools, and a PSE solver (PSE-Chem) which includes the effects of finite-rate chemistry and translational-vibrational exchange. The power of the STABL suite comes from its ability to quickly script and perform PSE analysis in parallel allowing for rapid assessment of linear stability for boundary layers for various axisymmetric and plane symmetric flows. Additionally, the software has the ability to extract mean-flow profiles to compare computed results against canonical transition correlations.

A typical workflow using STABL goes as follows. For conical flows, a grid is first

generated using the suite's automatic grid generation tools. A base flow is then obtained using the built-in Navier-Stokes solver. Once a mean flow is obtained, stability analysis is performed using the PSE-Chem solver. The modular nature of the STABL suite allows for solutions to be imported from other solvers or more complex flow fields for stability analysis.

3.6 Global Mode Analysis in US3D (GMAUS3D)

Certain flow configurations break the underlying assumptions that are essential to local and non-local approaches. For these cases, global mode analysis may be beneficial in assessing flow stability. In this work, A fully three-dimensional solver has been developed within the US3D framework for this reason. The software is named Global Mode Analysis in US3D (GMAUS3D). In addition to the exploiting the underlying data structures within the US3D solver, additional external libraries have been included for the solution to large sparse linear systems as well as iteratively solving for eigenvalues. The result is the ability to solve for global modes on structured, unstructured, and hybrid mesh topologies. Fig. 3.2 shows an unstructured mesh topology containing both hexahedral and tetrahedral elements and a global mode obtained on the unstructured mesh.

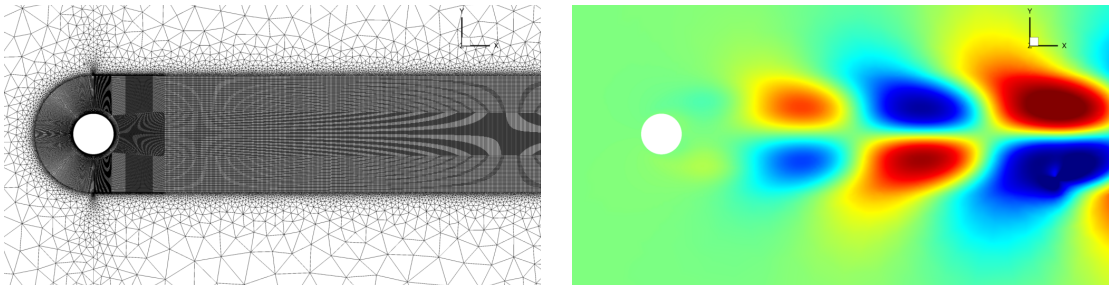

(a) Unstructured Mesh

(b) Resolved Unstable Global Mode

Figure 3.2: Unstructured mesh topology for cylinder wake flow.

GMAUS3D solves for the eigenvalues and eigenvectors of the global linear operator describing the Linearized Navier-Stokes disturbance equations. The global operator can be constructed in many ways. Building the global operator and associated boundary conditions explicitly can be cumbersome and prohibitively complex when linearizing limiters and switches within the non-linear code. Instead one may wish to use the linearized fluxes and associated face Jacobians to build the linear operator. Referring back to section 3.3.2, we found that the Modified Steger-Warming fluxes produced inviscid face Jacobians. This linearization is similar in fashion to what we wish to derive for the global linear operator, however an issue arises from the approximate nature of the viscous Jacobians (depending on what form of gradient reconstruction one uses). Linear stability analysis is highly sensitive to numerical dissipation (eigenvalues may be artificially damped/amplified due to poor approximations in the Jacobians). Additionally, no information on limiter and flux scheme switching functions is built directly into the face Jacobians, but rather it comes as a secondary step.

A remedy to these issues is to construct the linear operator through the computation of what is known as a numerical Jacobian. For small enough problems, explicit extraction and storage of the global operator is possible. The advantage of the explicit storage

of the operator is the ability to perform shift-invert strategy to probe specific portions of the eigenspectrum (reducing the overall number of operations to extract eigenvalues within a frequency range). Additionally, direct access to the adjoint through the definition of an inner-product allows for non-modal analysis as a natural extension. Due to the discretization scheme used for the work presented here, the global operator is sparse. With a plethora of sparse solver libraries available to the public, it was chosen that the matrix be extracted and stored explicitly for the work presented in this thesis.

3.6.1 Extraction of the Numerical Jacobian

The computation of the numerical Jacobian provides a means to extract the global linear operator (and associated limiter-influences) out of a non-linear CFD code. The process is straightforward. If we consider our CFD code to be a black box which produces residual vectors at each time step, we can write the governing equation (Eq. 3.6) as ,

$$\frac{dU}{dt} = \mathcal{R}(U) \tag{3.17}$$

Here $\mathcal{R}(U)$ represents the residual vector that is produced by the code. This vector represents the change in the fluid system at the current time. We can linearize this vector by performing a Taylor-Series expansion about a small perturbation in the conserved vector U,

$$\mathcal{R}(U + \epsilon u) = \mathcal{R}(U) + \epsilon \frac{\partial \mathcal{R}}{\partial U} u + \mathcal{O}(\epsilon^2)$$

Rearranging the above equation and neglecting nonlinear terms ($\mathcal{O}(\epsilon^2)$), we arrive at an expression for the linear operator to first order,

$$\mathbf{A} = \frac{\partial \mathcal{R}_i}{\partial U_j} = \frac{\mathcal{R}_i(U_k + \epsilon u_j) - \mathcal{R}_i(U_k)}{\epsilon u_j} \tag{3.18}$$

and second order,

$$\mathbf{A} = \frac{\partial \mathcal{R}_i}{\partial U_j} = \frac{\mathcal{R}_i(U_k + \epsilon u_j) - \mathcal{R}_i(U_k - \epsilon u_j)}{2\epsilon u_j} \tag{3.19}$$

The resulting equations show how to obtain the numerical Jacobian using small perturbations to the base flow. The non-linear solver is called with an additional perturbation for each degree of freedom at a time, and the entries in the Jacobian matrix are filled. Once completed, the global linear operator is consistent with the discretization, boundary conditions, and numerical schemes that were used to converged the underlying base flow. This approach is straight forward to implement, but has two main challenges. First, the choice of ϵ must be carefully selected to ensure the accuracy of the approximate Jacobian. Choosing too small of an ϵ can corrupt the approximation due to round-off errors, while values too large will violate the assumption of negligible nonlinear terms. Typically, we define $\epsilon = 10^{-6} U_{ref}$, where U_{ref} is a baseflow quantity. Second, the approach as defined is prohibitively expensive to compute (order N^2 CFD residual vectors required to build the matrix, where N is the total number of degrees of freedom). Instead, one can exploit the underlying sparsity of the operator due to the discretization of the underlying numerics.[1]

Given a single element i, Fig. 3.3 shows in two dimensions the cells for which the solution in cell i depends. This is known as a stencil. We can use this information to perturb multiple cells at a given time as long as the stencils of the cells for which we perturb are non-overlapping. The method is similar to Nielsen *et al.* [47] greedy algorithm.

[1] This approach will work for compact stencils but will not work for "compact" schemes such as ones proposed by Lele [46]

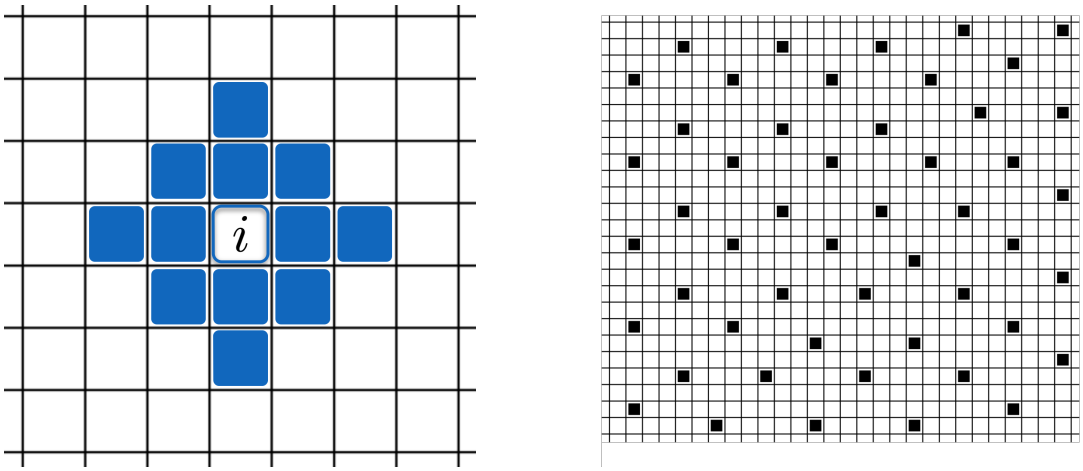

(a) Stencil for cell i

(b) Non-overlapping cells to be perturbed

Figure 3.3: Local stencil for cell i and 2-D mesh of non-stencil-overlapping cells that are allowed to be simultaneously perturbed.

Parallelization of the algorithm is straight forward, although the relative efficiency as compared to the method described by Nielsen *et al.*[47] is somewhat diminished. In the current case, each processor is allowed to fill the its domain with non-overlapping cells to be perturbed. The boundaries are then looped over to search for cells that overlap across processor boundaries. In the event a cell's stencil overlaps another stencil located on a different processor, the lower rank processor removes this cell from the current perturbation level and will be added in the next level. This approach is displayed in Fig. 3.4 a) and b), which shows the initial filling and correction for overlapping cells on 8 processors. The resulting total number of residual evaluations required is anywhere between 30 and 50 perturbations per equation for a given three-dimensional grid.

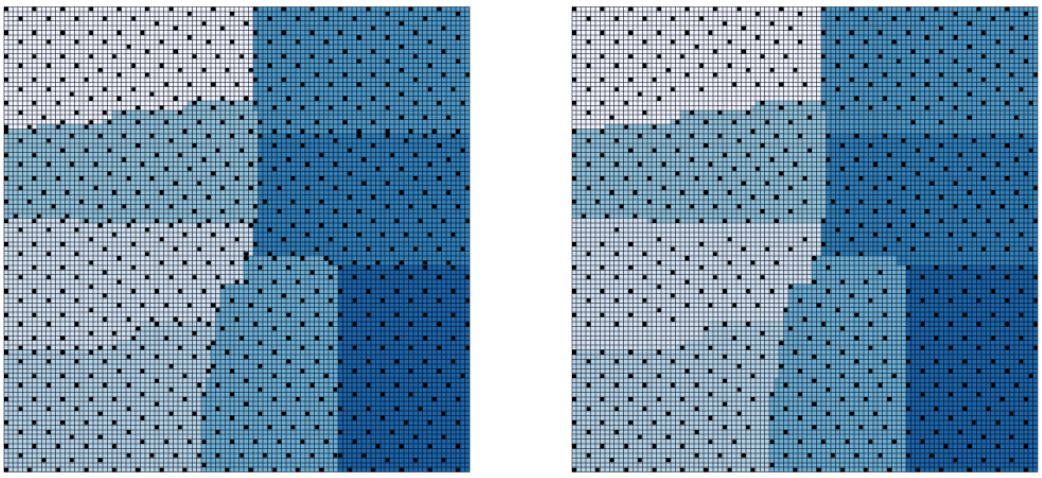

(a) Initial filling of domain for each processor

(b) Resulting allowable perturbations after removal of offending cells across processor boundaries

Figure 3.4: Two-dimensional computational grid.

3.6.2 Effect of limiters

When evaluating the numerical Jacobian, strong gradients in the flow variables can cause limiters to flip between low and high-order flux schemes sporadically. The underlying limiter must be smooth in order to prevent discontinuities in the Jacobian. This effect is most pronounced for supersonic flows. Consider the generic blunt body in supersonic flow seen in Fig. 3.5, with freestream conditions in Table 3.1. The computational mesh, Fig. 3.5 (a), contains roughly 22,000 elements (138x158 cells in the streamwise and wall-normal directions, respectively). Fig. 3.5 (b) shows the freestream-velocity (streamwise) component. The flow is dominated by a strong detached bow-shock.

Table 3.1: Freestream Conditions

Mach	V_∞ (m/s)	ρ_∞ kg/m^3)	T_∞ (K)
8.00	1207.9	2.5926×10^{-2}	56.739

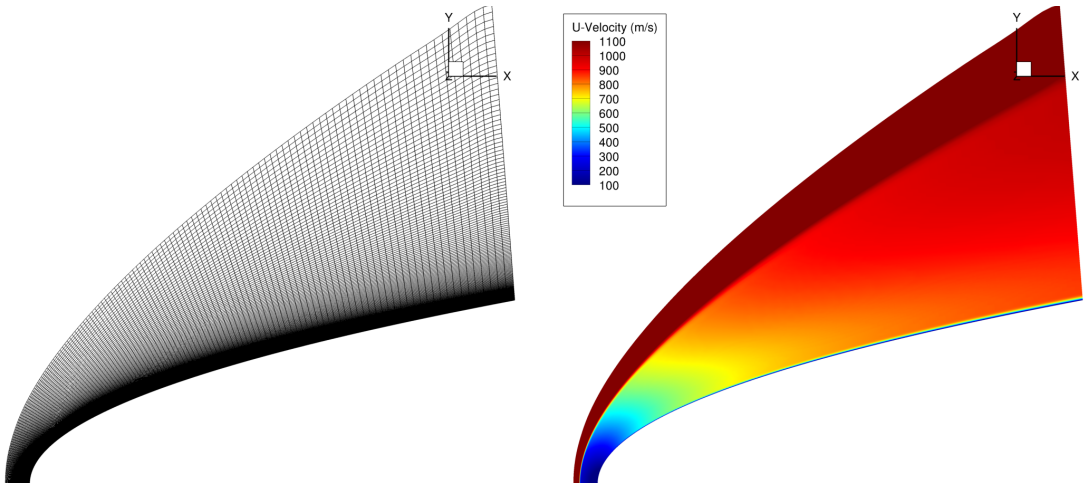

(a) Mesh (b) V-Velocity

Figure 3.5: Blunt body geometry in supersonic flow. This geometry serves as an example of a flow where limiters are active.

To assess the smoothness of the resulting Jacobian matrix, one can employ row-summation to see the effect of each row contribution on a solution vector. Consider the matrix below. Row summation is performed by adding the contribution from each column in an individual row (highlighted in red). The result is then a scalar contribution from the sum of $\sum (a_{i,1} + \cdots + a_{i,i} + \cdots + a_{i,N})$ to the degree of freedom v_i.

$$\begin{pmatrix} v_1 \\ \vdots \\ v_i \\ \vdots \\ v_N \end{pmatrix} = \begin{pmatrix} a_{1,1} & \cdots & a_{1,N} \\ \vdots & \ddots & \vdots \\ \sum(a_{i,1} & \cdots\ a_{i,i}\ \cdots & a_{i,N}) \\ \vdots & & \vdots \\ a_{N,1} & \cdots & a_{N,N} \end{pmatrix}$$

Fig. 3.6 a) and b) show two limiters implemented in US3D (Min-Mod and Van-Albada 1, respectively). We can see that the first derivative of the Min-Mod limiter function is not smooth. This can create problems when evaluating the numerical Jacobian using the perturbation method described in the previous section. If the small ϵ value is large enough, or the solution region is sensitive enough, the addition of the perturbation can cause the limiter to become active in a localized region creating non-smooth Jacobian contributions. Fig. 3.6 c) and d) show the U-momentum contribution to a solution vector. The effect of the limiter switching between high and low-resolution schemes can be seen in the shock layer for the Min-Mod case, while the Van-Albada produces a smoothly varying function within the shock layer. Both limiters are active within the shock causing non-smooth variations. This can be due to shock misalignment.

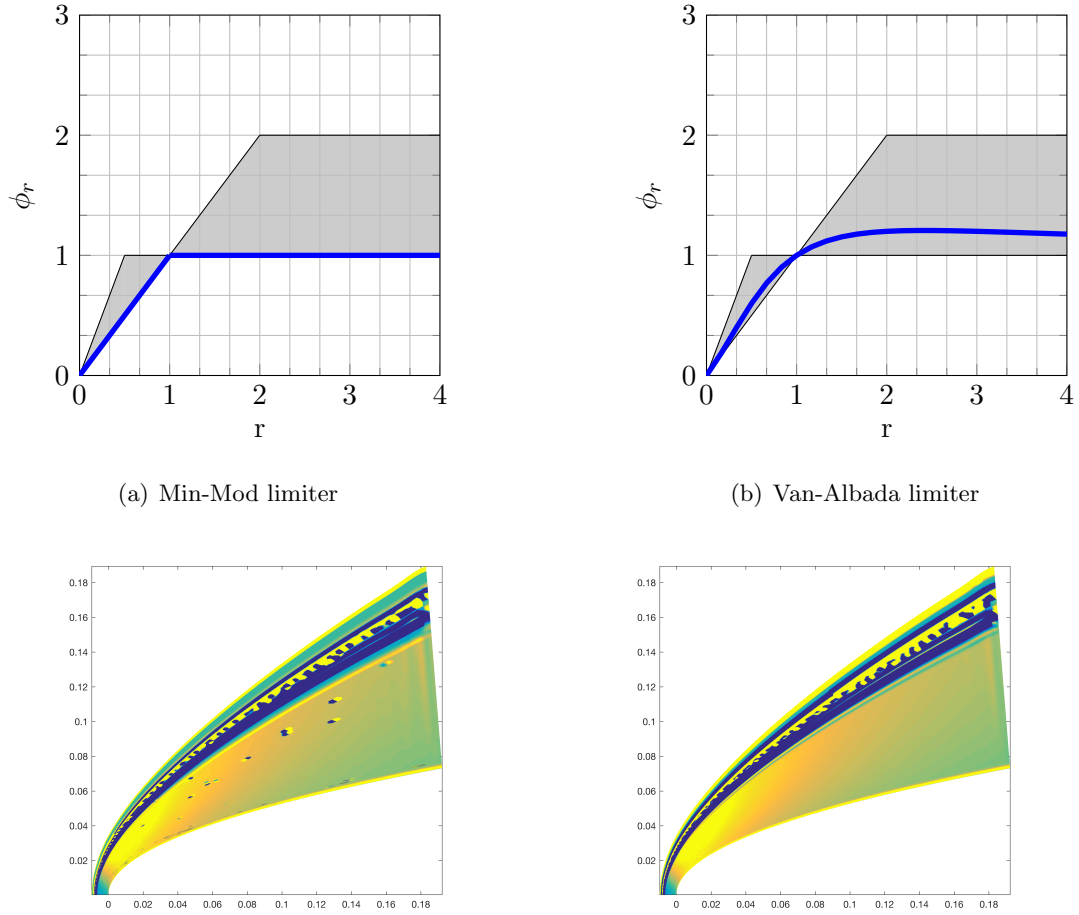

(a) Min-Mod limiter

(b) Van-Albada limiter

(c) U-Momentum using Min-Mod

(d) U-Momentum using Van-Albada

Figure 3.6: U-momentum contribution of linear operator.

3.6.3 Solution Methodology

Returning to the governing equation for linear disturbances 2.3, we cast the system as an eigenvalue problem using the TriGlobal decomposition described in the previous

chapter. The resulting Ansatz becomes,

$$\omega \mathbf{q} = \mathcal{A}\mathbf{q} \tag{3.20}$$

Here, ω is a complex eigenvalue of global linear operator $\mathcal{A}$, and $\mathbf{q}$ is the complex eigenvector. Eq. 3.20 can be solved using either direct or iterative methods. three-dimensional hypersonic base flows often require large resolved meshes. This results in a large eigenvalue problem to be solved. For this reason, GMAUS3D uses the Implicitly Restarted Arnoldi Method (IRAM) implemented in the open-source software PARPACK (parallel version of ARPACK) [48]. The effect of compressibility in addition to three-dimensional base flows can produce rich/complex eigenvalue spectra. In order to efficiently probe the eigenvalue spectra, the use of the shift-invert mode available in the software is chosen to converge a small subset of the global spectrum. The eigenvalue problem (Eq. 3.20) is augmented by a shift value σ,

$$(\omega - \sigma)\mathbf{q} = (\mathcal{A} - \sigma I)\mathbf{q} \tag{3.21}$$

Eq. 3.21 is then inverted resulting in,

$$\mu \mathbf{q} = (\mathcal{A} - \sigma I)^{-1}\mathbf{q} \tag{3.22}$$

This operation results in eigenvalues ω near the shift value σ to have the largest magnitude μ. The shift-invert mode allows for different regions of a given spectrum to converged rapidly when using an iterative Arnoldi method. The requirement for this type of approach is either a direct inversion or a linear solve of the operator $(\mathcal{A} - \sigma I)^{-1}$.

The formulation of Eq. 3.22 results in linear solver step per Arnoldi vector. For small enough problems, the matrix can be formed explicitly and factored allowing for a direct solve. This results in fast linear solves but large memory overhead. For the smaller problems presented in this thesis, direct solves were carried out using SUPERLU_DIST

software [49], with the parallel symbolic factorization [50]. The total memory overhead for a full three-dimensional solve results in a memory cost around 50 times that required to store the original sparse matrix due to the fill-in for the LU factorization. This limits the size of the problems to be less than 10^7 degrees of freedom. Larger problems will need to be solved using iterative solvers.

Chapter 4

Code Verification

Before we can move forward with the stability analysis of relevant base flow configurations, we must first verify the global linear operator within GMAUS3D.

The first case presented will be the global stability analysis of a super critical Reynolds number cylinder wake flow. This test case is considered a fundamental configuration. The geometry results in a base flow that is not consistent with the underlying assumptions of local/nonlocal stability approaches and is considered ideal for global stability analysis. Results obtained by GMAUS3D will be presented and the leading unstable eigenvalue will be compared against values in literature.

The second configuration will be a supersonic blunt cone. The resulting base flow is consistent with the underlying assumptions of the parabolized stability equations (PSE). The goal is not to out perform the simplified (less computationally expensive) linear analysis techniques of LST and PSE, but rather to compare the results obtained by the TriGlobal analysis approach implemented in GMAUS3D. Key differences in the obtained eigenvalue-spectra and overall meaning will be discussed.

4.1 Cylinder Wake

The vortex shedding behind a circular cylinder is considered a canonical base flow in the considerations of global-instability analysis. Early analysis of this problem dates back to the early works of Jackson [51], Zebib [52], and Hill [53]. In order to verify the extracted matrix contains the correct global matrix that represents the base flow physics, we compare the computed unstable eigenvalues obtained using GMAUS3D to the results published by Crouch *et al.* [54] for 5 mesh sizes.

4.1.1 Computational Mesh

The various mesh sizes used can be seen in Fig. 4.1. The computational meshes are constructed such that the refinement is localized to the wake region and stretched as you move away from the cylinder. Because the baseflow is subsonic, we need to ensure there will be no reflections of disturbances within the domain. This can either be done by imposing a numerical sponge layer or stretching the computational mesh to reduce the resolution in the far-field regions. For all cases here, the outer boundary is stretched approximately 125 diameters away from the cylinder with cell sizes many times larger than the cylinder. This produces a sponge region due to the coarseness of the mesh.

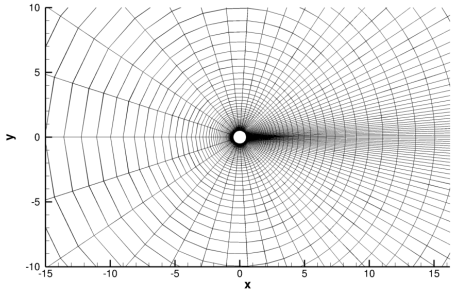

(a) 80x80

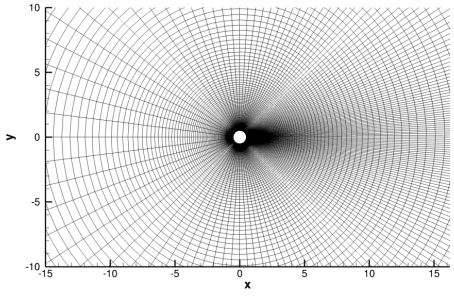

(b) 160x160

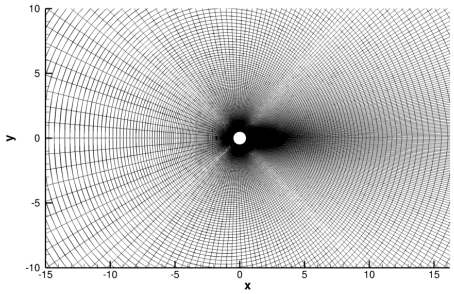

(c) 240x240

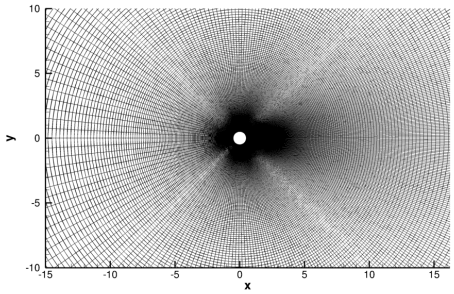

(d) 320x320

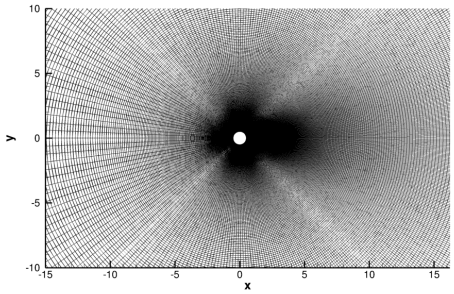

(e) 400x400

Figure 4.1: Various mesh sizes used in verification.

4.1.2 Baseflow

Contours of u-velocity can be seen in Fig. 4.2 for a Reynolds number of 60 and Mach number of 0.2.

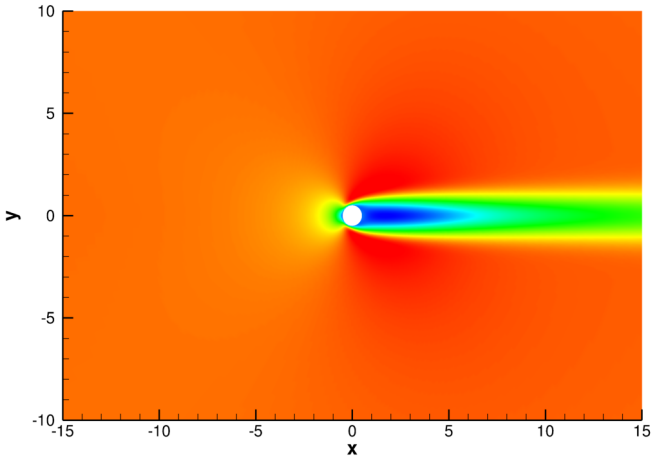

Figure 4.2: Base flow of cylinder wake with contours of streamwise velocity. $M = 0.2$ Re= 60

The free-stream conditions for the cylinder base flow can be seen in Table 4.1 below;

Table 4.1: Cylinder Baseflow Freestream Conditions

Re	U_∞ (m/s)	ρ_∞ (kg/m^3)	T_∞ (K)	Mach
60.0	69.4377	1.200	300.0	0.2

In order to achieve a Reynolds number of 60 with the above free-stream conditions, one must augment the chosen viscosity model. The viscosity model used in the calculation of the base flows here is the Blottner viscosity curve fit model[55]. The model is expressed as an exponential function with coefficients A, B, C and translational temperature T_{tr}.

$$\mu = 0.1 \exp\left[(A \ln \mathrm{T}_{tr} + B) \ln \mathrm{T}_{tr} + C\right]$$

Setting coefficients A and B to zero and $C \approx 2.631$ results in a viscosity that yields a free-stream Reynolds number of 60. The Reynolds number for this flow is considered super-critical meaning the flow will become unstable due to small perturbations and vortex shedding will occur. To prevent this, the baseflow was initialized with dissipative numerics in both the spatial and temporal sense to damp out any perturbations.

4.1.3 Global Mode Analysis

As mentioned earlier in section 3.6, the construction of the global linear operator can have significant consequences on the approximated eigenvalues. A comparison of the linear operator constructed using the face Jacobians consistent with those from the Modified Steger Warming approach described in section 3.2.1 and one built using the numerical Jacobian approach can be seen in Fig. 4.3. There are many factors contributing to the large differences between the resolved eigenvalue spectra (approximate viscous Jacobians, numerical switches, boundary conditions, etc). Because the numerical Jacobian is consistent with the numerical methods and boundary conditions used in obtaining the underlying baseflow, it is able to reproduce the unstable wake mode as seen by the eigenvalue that lies above the complex half-plane ($\omega_i > 0$).

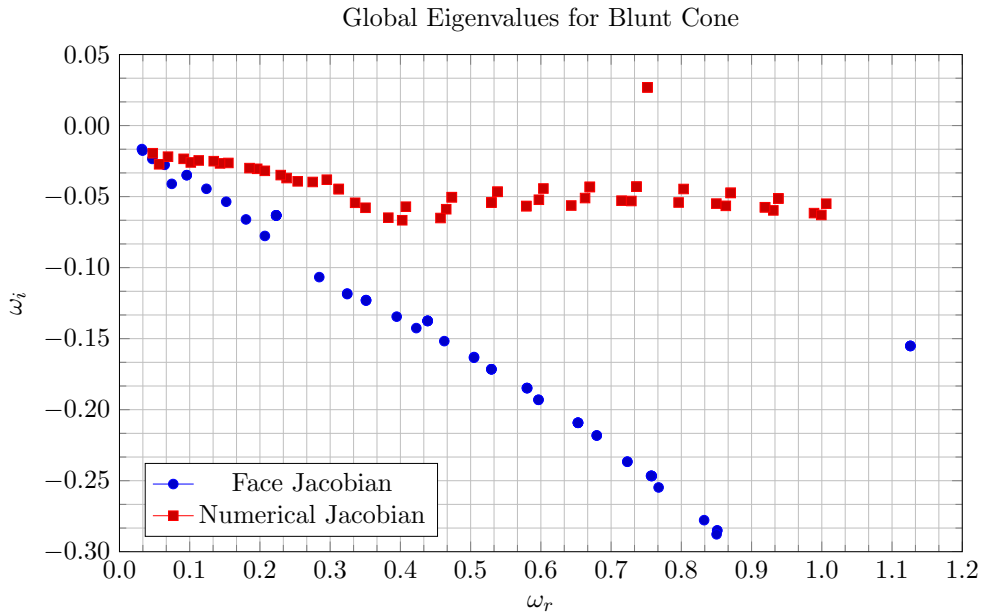

Figure 4.3: Comparisons of resolved eigenvalues for face-Jacobian vs numerical Jacobian matrices

A comparison of the unstable eigenvalue computed with GMAUS3D against the results of Crouch *et al.* can be seen in table 4.2. The values for the single unstable mode are within a reasonable range with literature. However, the results for GMAUS3D do not seem to converge to a specific value as they do in the cited literature. A potential reason may be due to the dissipative numerics used to force a stable solution. As the mesh becomes more refined, there is a competing effect between the numerics and mesh resolution of disturbances which can affect the convergence of the base flow. Additionally, further investigation is needed for the sensitivity of the eigenvalue spectra on the choice of ϵ used in the numerical Jacobian extraction, the number of Arnoldi vectors used in the IRAM methodology, and numerics used for the base flow solution.

Table 4.2: Unstable Eigenvalues for Cylinder at Re=60

Mesh	Least Stable ω [54] (Upwind)	Least Stable ω (Current)
$80x80$	$0.7564, 0.0277$	$0.7789, 0.0154$
$160x160$	$0.7425, 0.0418$	$0.7427, 0.0387$
$240x240$	$0.7396, 0.0433$	$0.7637, 0.0402$
$320x320$	$0.7386, 0.0437$	$0.7526, 0.0385$
$400x400$	$0.7382, 0.0439$	$0.7697, 0.0469$

Figure 4.4 shows the streamwise and spanwise velocity disturbances (u and v). The asymmetrical pattern in the streamwise velocity coupled with the oscillating spanwise velocity disturbance in the streamwise direction creates vorticity which acts to disrupt the smooth lamina of the shear layer and would contribute to the initiation of vortex shedding. Comparisons to literature and visualization of the unstable mode provide verification of the implemented linear operator for this subsonic case.

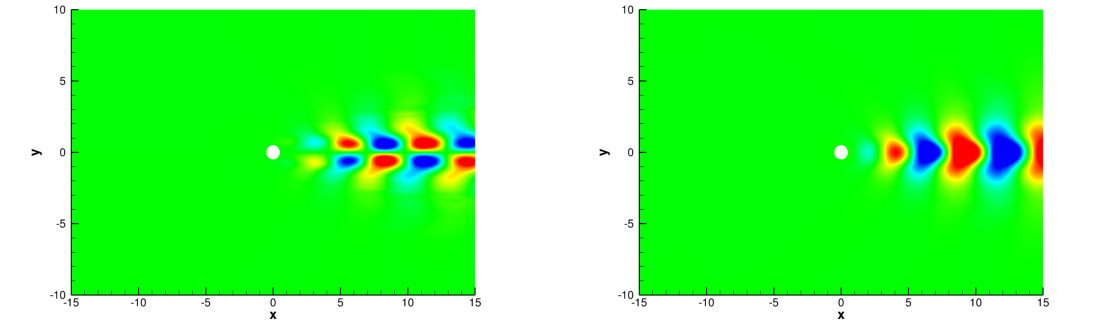

(a) Unstable $\hat{u}$-disturbance

(b) Unstable $\hat{v}$-disturbance

Figure 4.4: Global Modes for Cylinder Wake at Re = 60.

4.2 Supersonic Blunt Cone

Laminar-turbulent boundary layer transition for supersonic and hypersonic speeds presents consequences in addition to drag. Many high-speed vehicles are designed as long slender bodies to reduce drag, however at high-speeds the skin-friction and mixing of a turbulent boundary layer can greatly increase the acreage heating of the surface. Prediction of boundary layer transition can improve vehicle design.

To model high-speed transition on a simplified geometry, a blunt 75-degree cone will be used for the baseflow configuration. This geometry has been extensively studied using both local and non-local techniques described in section 2.3. The results are presented first for the STABL software suite. These results are presented within a spatial stability framework. The implications of this will be made clear once the results from GMAUS3D are presented. The comparison will be discussed.

4.2.1 Base Flow

The base flow for this geometry was obtained using US3D. As noted in literature, supersonic blunt cones with cold walls are often susceptible to boundary layer transition due to Mack's second mode [19] [56] [57]. Freestream conditions chosen to exemplify this are shown in Table 4.3.

Table 4.3: Blunt Cone Baseflow Freestream Conditions

U_∞ (m/s)	ρ_∞ (kg/m^2)	T_∞ (K)	Mach
1956.81	1.44×10^{-3}	255.56	7.99

Accurate LST and PSE analysis requires high quality meshes [58]. The mesh chosen for this work contains approximately $700,000$ cells. The domain extends from the blunt nose with radius approximately 2.5 mm centered at 0 to 1.7 meters downstream, presenting a problem of significant ranges in scale. Fig. 4.5 shows contours of temperature

and streamwise velocity for the blunt cone base flow. Similar to the cylinder case presented in the previous section, dissipative numerics have been chosen to model this base flow to ensure smooth laminar flow. Temporal integration was performed using first order DPLR with second order, upwinded Modified-Steger-Warming fluxes for spatial integration.

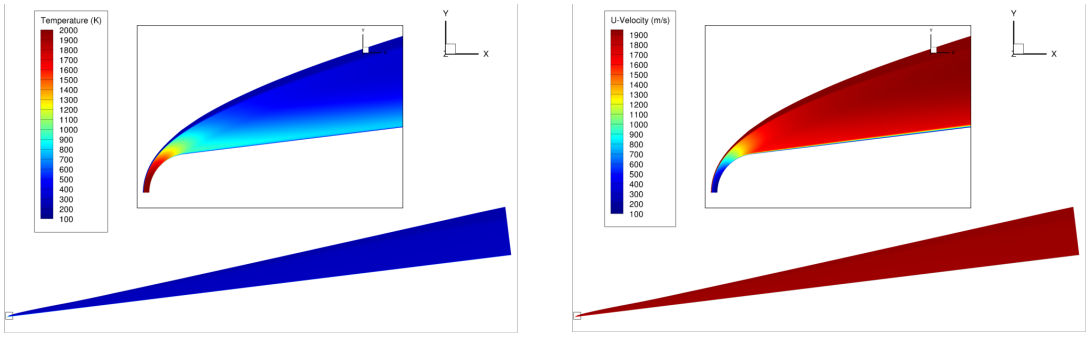

(a) Temperature Contours

(b) Streamwise Velocity Contours

Figure 4.5: Supersonic Blunt Cone Case.

4.2.2 STABL

Local (LST) and non-local (PSE-2D) modal stability analysis is implemented in the suite Stability and Transition Analysis for hypersonic Boundary Layers (STABL) [59]. The solver contains a two-dimensional finite-rate chemically reacting Navier-Stokes solver for producing the base flow. It can also handle 2-dimensional laminar base flows extracted from other solvers (US3D in this case). When invoking the PSE-method, the modal set of equations is solved in a similar fashion as described in Section 2.3.1. The result is amplification rates of disturbance frequencies known in literature as "N factors". For all results, an assumption of $\beta = 0$ has been made due to the primary instability

being acoustic planar waves. Additionally, when employing global analysis on a two-dimensional plane, an implicit assumption of $\beta = 0$ is made. Therefore these results will be better compared to global results later in the section.

Fig. 4.6 shows the stability analysis generated by STABL. The figure on the left shows results generated using LST. Plotted are contours of amplification rates, α_i. The narrow band of positive α_i indicates an unstable mode at the given downstream location for the given frequency. The graph on the right is the result of PSE analysis. The plot shows curves of N-factors (for a given frequency) vs downstream distance. Highlighted in red is the first N-factor to achieve a value greater than 7 (an engineering correlation assumed to be the onset of transition).

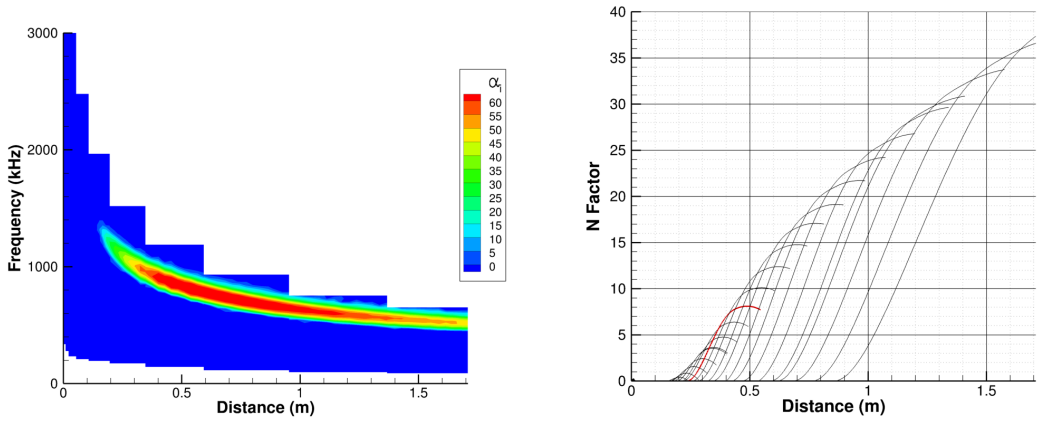

(a) LST Diagram

(b) N-Factor Results from PSE

Figure 4.6: STABL Results.

Together, these results tell us the frequency range for which small amplitude disturbances grow and where they become unstable. Additionally, the N-factor curves give insight into the downstream evolution of a disturbance for a given frequency. This methodology has proven useful and efficient for assessing stability on slender bodies.

4.2.3 GMAUS3D

STABL offers the computational advantage over GMAUS3D for simple two-dimensional flow fields due to the lower computational cost of the implemented LST and PSE methods as compared to the TriGlobal method. It is important to note that the comparison between the TriGlobal analysis of GMAUS3D for a two-dimensional mesh is similar to a BiGlobal approach with a spanwise wave number equal to zero. This section is not meant to show an improvement over the current tool. Instead we focus on showing how can global modes can be used in a predictive sense for stability.

Modal Results

Modal analysis of the supersonic base blunt body flow results in the eigenvalue spectra shown in Fig. 4.7. The low-frequency range results in two distinct branches that coalesce as the frequency increases. All eigenvalues lie below the complex half plane $\omega_i = 0$, indicating stable global disturbances. The structure of the global modes can differ greatly between the frequency ranges.

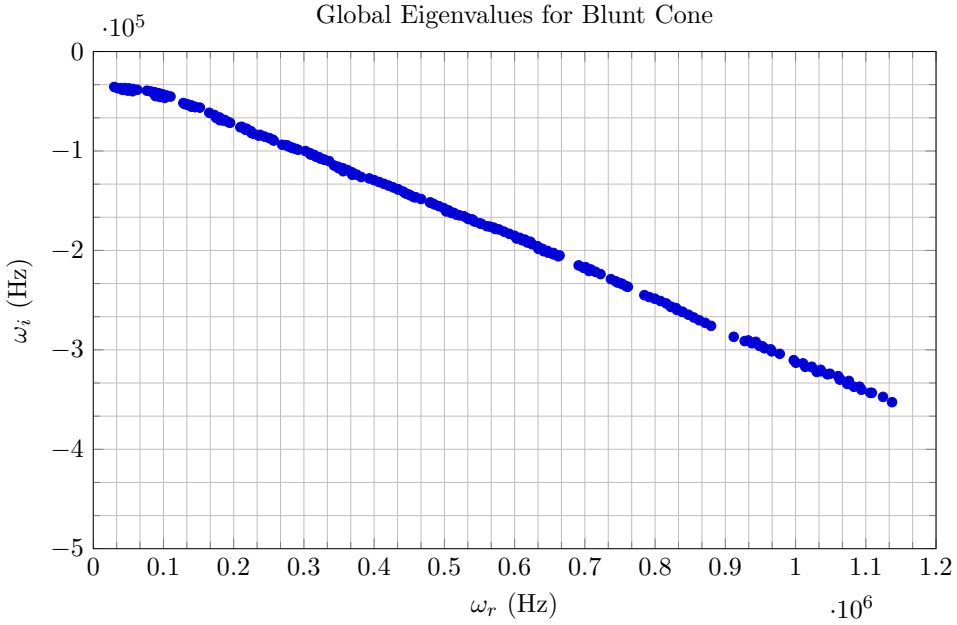

Figure 4.7: Eigenvalue spectra for supersonic blunt cone.

Fig. 4.8 shows the low frequency (indicated by the red arrow above) and a moderate frequency mode (indicated by the dashed green arrow above). Both modes appear at the downstream end of the domain.

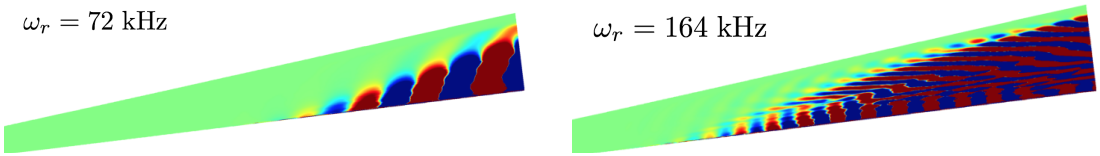

(a) low-frequency $\hat{u}$-mode (b) moderate-frequency $\hat{u}$-mode

Figure 4.8: Global modes.

The high-speed boundary layer produces instabilities which travel in the flow direction. Unlike the spatial stability analysis used in STABL, global modes are defined in a temporal stability fashion. Due to the convective nature of the high-speed boundary layer, disturbances may amplify in space, but in time are convected out of the domain and are thus stable in the long time (Lyapunov) stability sense. In terms of (Bi)Global stability, the present flow is stable to the resolved frequency range.

Non-Modal Analysis

For the given baseflow configuration, the temporal formulation of global stability analysis produces stable global modes due to the convective nature of the baseflow. In an effort to directly compare computed global modes with the spatial stability analysis of classical methods, we can leverage the computed global modes to solve for the short time amplification due to their non-normal character. The short-time amplification can produce a wave packet with a spatial structure consistent with the N-factor results from the previous section.

We first derive a method to solve for the short time amplification for a superposition

of global modes. This method is similar to the one defined by Ehrenstein et al [60]. Consider the eigenvalue problem

$$\lambda \mathbf{q} = \mathbf{A}\mathbf{q}.$$

We can define a set of eigenvectors q as a large matrix of eigenvalues Q with an associated diagonal matrix Λ containing individual eigenvalues.

$$\Lambda \mathbf{Q} = \mathbf{A}\mathbf{Q}$$

Defining a Hermitian matrix based on the L2 inner product of the global modes, $M = Q'Q$, we can perform a Cholesky decomposition of M as,

$$M = F^H F$$

Taking the product of F and F^{-1} with the matrix exponential of the diagonal matrix of eigenvalues Λ, we can define a superposition of global modes by,

$$B = F \exp(t\Lambda) F^{-1}$$

Taking the singular value decomposition, $B = U^H \Sigma V$, and taking the v_1 input mode, which corresponds to the largest singular value, σ, results in an optimal initial disturbance for the superposition set B. Maximizing the initial condition v_1 over a time interval produces the maximum possible growth for the given set of global modes. The optimal superposition of global modes is expressed as, $q_{\text{opt}} = QBv_1'$. Fig. 4.9 shows the energy amplification for an optimal superposition of global modes.

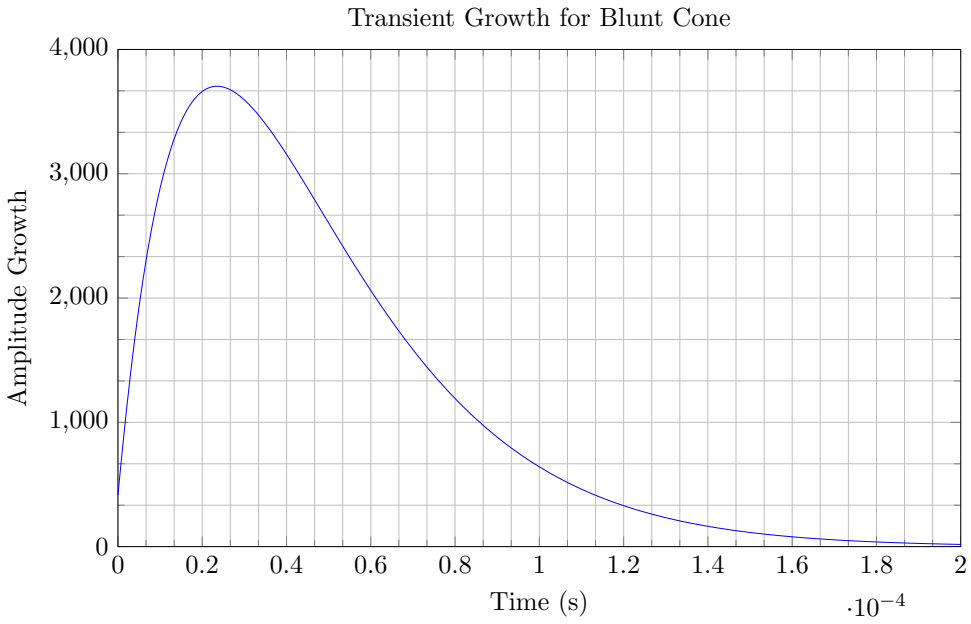

Figure 4.9: Energy amplification.

The spatial structure of the optimal superposition exhibits spatial growth of the amplitude in the downstream direction due to the convective nature of the boundary layer. The amplitude of the optimal structure at a given downstream location may be defined as,

$$A(x) = \sqrt{\int_0^H Q'WQ\mathrm{d}y}$$

Where W is the weight matrix which defines the norm. In this case, we take $W = I$ and the resulting norm is the L-2 norm. This function may be compared to the classical e^N method as,

$$\frac{A(x)}{A(0)} \approx \mathrm{e}^N.$$

Fig. 4.10 shows the comparison between the computed N-factors of STABL and the

streamwise optimal global mode growth computed with GMAUS3D. The shape of the N-factor curve shows a similar "s"-shape for both STABL and GMAUS3D. Given the underlying dissipative numerics used to obtain the smooth baseflow, and the difference between optimal input-disturbances from GMAUS3D versus the frequency response envelope provided by STABL, the comparison between the two methods is highly encouraging.

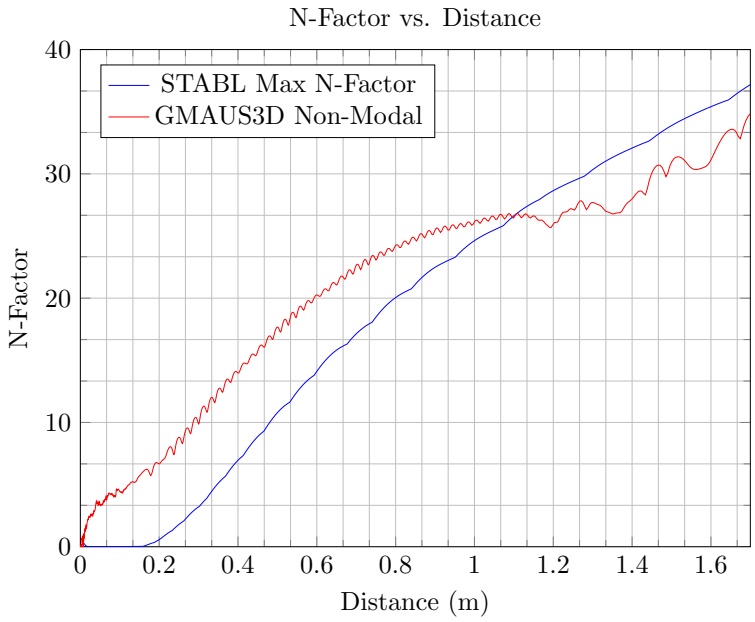

Figure 4.10: Maximum N-Factor produced by STABL vs non-modal energy amplification of optimal disturbance from superposition of global modes produced by GMAUS3D.

4.3 Review

Development and application of Global mode Analysis in US3D (GMAUS3D) has been applied to a subsonic cylinder test case. Comparison of the linear operator built with face Jacobians from the Modified-Steger-Warming fluxes and the extracted numerical

Jacobian showed significant differences in the resolved eigenvalue spectra. The numerical Jacobian was able to recover the unstable eigenvalue for this canonical flow, while the face Jacobian matrix was significantly damped. When comparing the unstable eigenvalue for 5 different mesh resolutions, results showed good agreement as compared to literature.

Global mode analysis was also applied to a supersonic blunt cone. The eigenvalues produced were all stable. It was reasoned that the convective nature of the high-speed boundary layer acts as an amplifier to disturbances in a spatial framework, but will convect the instability out of the domain and thus be stable in a temporal view. In order to obtain good comparison with spatial stability analysis, non-modal analysis was introduced to assess the short-time amplification of disturbances. The result was able to recover the spatial behavior of disturbances in global modes with a similar profile as STABL.

Chapter 5

Conclusion and Discussion

Understanding the physics of small scale disturbances with the capability to amplify can lead to a better understanding of transition mechanisms. Geometries with relatively simple/smooth OML can produce complex three-dimensional boundary-layer profiles which render classical approaches invalid. With the increase in computational power over the past decade, global methods are now a feasible approach to stability analysis. This dissertation introduced a triglobal analysis tool GMAUS3D, developed within the unstructured Navier-Stokes solver US3D. This section will summarize the results/discussion presented in previous chapters as well as propose extensions to this research and introduce new software which is already in development.

Chapter 1 introduced and motivated the study of transition in high speed boundary layers. With poor understanding of transition mechanisms, the use of thermal protections systems (TPS) can result in over conservative designs and greatly increase cost or reduce scientific payload. A history of classical methods was briefly introduced and a few of the many great papers were referenced. A seemingly simple geometry was introduced to exemplify a geometry for which the resulting base flow contained regions in which classical stability approaches failed.

Chapter 2 introduced the basic concepts for performing linear stability analysis. First the governing equations for fluid flow, the Navier-Stokes equations, were introduced. The equations were then modified by assuming a base state (which is assumed steady throughout this dissertation, but need not be) plus a perturbation. With this modification, the linear disturbance equations are then introduced. These equations are the basis of linear analysis. A range of modal assumptions and their resulting nomenclature, physical meaning, and numerical consequences were introduced. Classical local and nonlocal approaches were discussed (LST and PSE, respectively). Global analysis was then introduced starting first with BiGlobal analysis, then PSE3D, and ending with the most general modal analysis technique TriGlobal analysis.

The system of equations resulting from the modal assumption results in an eigenvalue problem. A standard technique for solving an eigenvalue problem is first presented as a mathematical baseline. Due to the large computational cost of direct methods associated to the global linear operator, the popular iterative approach provided by the Arnoldi method is introduced and discussed.

With an understanding of the resulting system of equations needed to be solved in an EVP form and the presentation of a solution methodology available in the Arnoldi method, Chapter 3 introduces the numerical approach. The first part of the chapter discusses the finite volume method. The finite volume method is the numerical discretization that is used for both US3D and GMAUS3D. The capabilities of US3D are briefly presented. Then a description of how the linear analysis is performed within the US3D framework is presented.

A method for obtaining the global linear operator is first introduced. Obtaining the global linear operator is achieved by the evaluation of a numerical Jacobian. This approach is similar to a central differencing scheme. The consequence of this approach is the seemingly arbitrary choice of the perturbation scaling parameter ϵ. For values too small, the approximation is corrupted by round-off errors, while large values result

in poor approximation. Following the mathematical derivation, a brief explanation of the implementation of the method and its extension to multiple processors is presented and discussed.

Following the description of the matrix extraction approach, the linear modal analysis solver, GMAUS3D is introduced. GMAUS3D stands for Global Modal Analysis in US3D. This code exploits the underlying data structures present within US3D to perform stability analysis on a given base flow. An overview of the included libraries and code structure follows.

Chapter 4 covers the verification cases chosen for this analysis. The subsonic cylinder wake is considered a classic base flow chosen for stability analysis due to the unstable wake for flows above a critical Reynolds number. This is known as Hopf bifurcation and is due to an amplification of an unsteady disturbance mode in the wake of the cylinder. The result is a break down of the steady symmetric wake resulting in the Von-Karman vortex street downstream. An assessment on the matrix formulation was made in order to motivate the usage of the numerical Jacobian procedure described in earlier sections. Global stability analysis was performed on 5 different levels of mesh refinement. The resulting unstable eigenvalue was compared against literature and found to be in good agreement.

The second case considered was a supersonic blunt cone. This geometry represents many slender bodies which experience high-speed boundary layer transition. It has also been extensively studied with classical techniques such as LST and PSE. This section presents LST and PSE analysis performed with the boundary layer transition suite STABL. Global mode analysis is then presented. All eigenvalues recovered are found to be stable. An explanation for this is given and non-modal analysis is introduced as an extension to current findings. After manipulation, non-modal analysis using the global modes generated by GMAUS3D recover similar behavior in the predicted N-factor for the cone as compared to STABL.

5.1 Extensions to Current Research

The development of the global mode analysis software GMAUS3D opens the way for the study of more complex flows where classical methods break down. The use of this tool will enable additional avenues of investigation of transition mechanisms. This section illuminates some potential areas of future investigation and attempt to identify possible difficulties therein.

5.1.1 BiGlobal Analysis on HIFiRE-5

As mentioned in the introduction, three-dimensional boundary layer transition offers a complex and interesting problem to the study of boundary layer stability. Where classical methods are limited, such three-dimensional boundary layers, global analysis can provide the capability to predict stability. The elliptic cone geometry studied here is be based off the Hypersonic International Flight Research Experimentation (HIFiRE) 5 flight experiment configuration. The HIFiRE program was developed jointly between the United States Air Force Research Laboratory (AFRL) and the Australian Defense Science and Technology Organization as the primary drivers. Several universities, private companies, and NASA have contributed greatly to the research of the program. The HIFiRE program couples flight experimentation to basic hypersonic transition research concepts. While the HIFiRE-1 program focused on an axisymmetric vehicle, the HIFiRE 5 program relies on an elliptical geometry.

Base Flow

The base flow is obtained using the US3D flow solver described in Chapter 3. The solution was obtained using second-order accurate Modified Steger-Warming fluxes. Time integration was carried out using second-order backward differencing formula. For the given trajectory, freestream enthalpy was insufficient to produce chemical or gas effects

allowing for single species perfect-gas to be used. The computational mesh contains 200 finite volume cells in the wall normal direction with complex mesh refinement in the streamwise direction to produce nearly isotropic cells in the spanwise and streamwise directions. The resulting computational mesh contains slightly more than 25 million elements. The flow can be seen in Figure 5.1 The reader is referred to Dinzl *et al.* [61] for more detail on mesh generation topology.

Freestream conditions are shown in Table 5.1 and correspond to High Reynolds number condition from Ref. [61].

Table 5.1: HiFIRE 5 Freestream Conditions

Re	U_∞	ρ_∞	T_∞
11.8×10^6/ m	869.7 m/s	4.6×10^{-2} kg/m^2	52.3 K

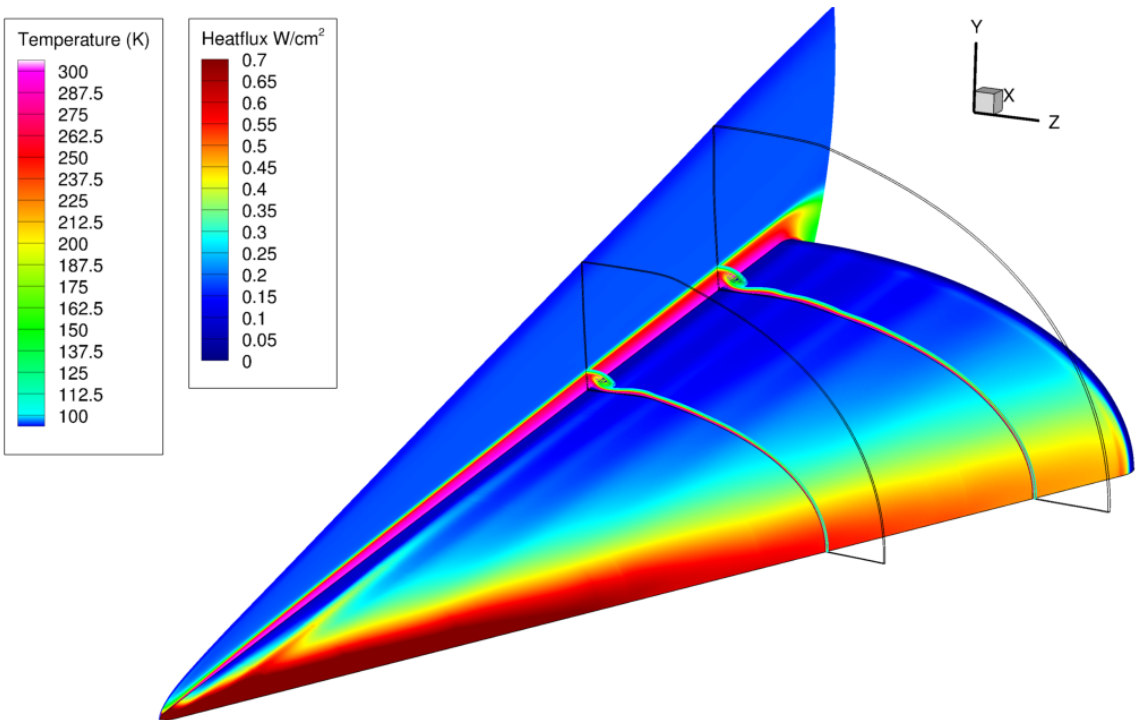

Figure 5.1: HIFiRE-5 Baseflow. Centerline and cross-plane slices show solid contour and contour lines of Temperature, respectively. The surface of the vehicle is contoured by heat flux.

Global Mode Analysis of HIFiRE-5 Geometry

Global mode analysis using direct solvers for the full 25 million element three-dimensional ellipse cone exceeds current computational capabilities. Since the current mesh level is already considered coarse, as compared to the DNS results by Dinzl *et al.* [61], reducing the mesh density further could affect the accuracy of the baseflow representation.

A potential solution to the memory requirement of direct solvers would be the solution of the linear system using an iterative approach. The solution to large sparse linear systems has been an active area of research in computer science. *"Finding a good*

preconditioner to solve a given sparse linear system is often viewed as a combination of art and science." -Saad [62]. While iterative solvers provide a lower computational cost, selecting an appropriate pre-conditioner remains a difficult task and is considered an important step in future development efforts.

An alternative to performing stability analysis on the full geometry, global mode analysis can be carried out on two dimensional planes within the base flow and three-dimensional subsection. This section serves as an example of the application of GMAUS3D to subdomains of complex geometries/flow configurations.

Cross Planes

Modal analysis for the cross plane sections produced zero frequency damped disturbances. These disturbances are considered to be stationary in time. It is interesting to plot the disturbances and the baseflow to see mode shapes/locations in response to baseflow structures. Fig. 5.2 shows two cross planes at locations $x/L = 0.7$ and $x/L = 0.9$ with contours of $\hat{v}$-disturbance (wall normal velocity perturbation). The positive (upward) and negative (downward) maxima appear to coincide with the streaks seen in the wall heat flux. These locations have streamwise vorticity which pushes hot fluid down into the boundary layer creating a hot region, or lift cool fluid up from the boundary layer producing cold regions. The streamwise vortices themselves lie between the maximum and minimum wall heat flux streaks. The perturbations are located between two adjacent streamwise vortices.

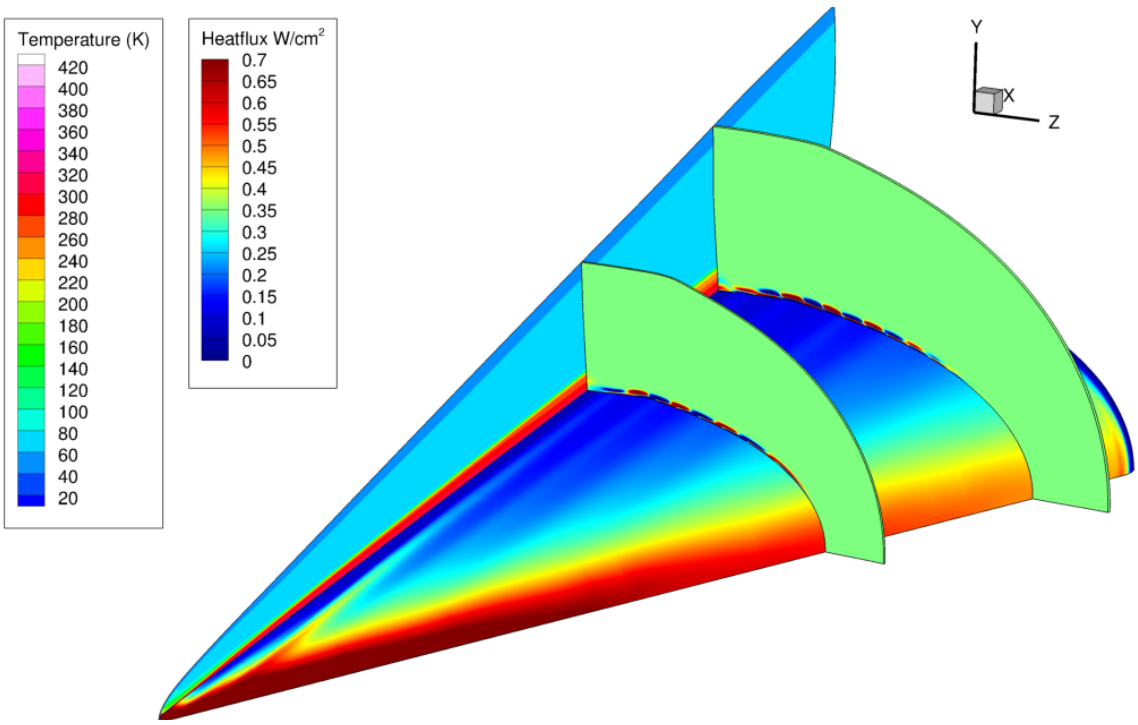

Figure 5.2: Centerline temperature and wall heat-flux contours of the baseflow with cross-sectional planes showing the $\hat{v}$-disturbance at $x/L = 0.7$ and $x/L = 0.9$.

A comparison of the disturbance profiles from the global results and the physical streaks seen in the experimental results by Juliano *et al.* [63] can be seen in Figure 5.3 (a) and (b). While the conditions are not exactly identical, the global analysis results are promising in their qualitative comparison to experimental results.

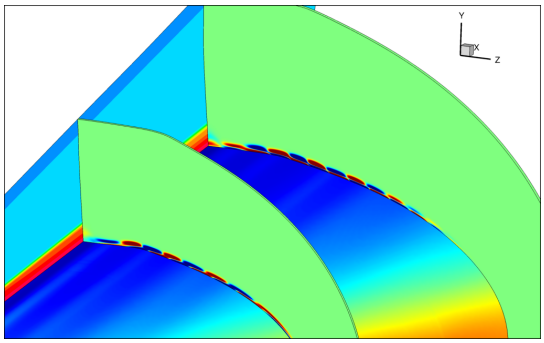

(a) Close up of the wall-normal-disturbance at locations $x/L = 0.7$ and $x/L = 0.9$.

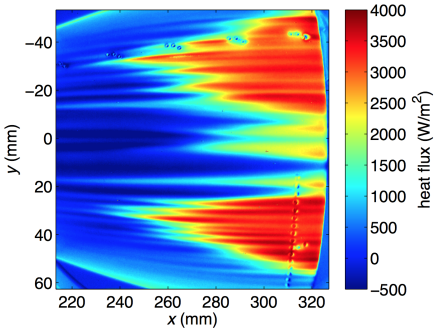

(b) Experimental Results for HIFiRE-5 by Juliano *et al.* [63].

Figure 5.3: Global Modes for cross sectional planes compared to streaks seen in experiment.

Three-Dimensional Subdomain TriGlobal Analysis

BiGlobal analysis offers an advantage over classical local approaches by solving for disturbance modes two-dimensional slices allowing for the mode shapes to cover more complex geometry. However, the third dimension is assumed to be described by parallel flow. This is not the case for the HIFiRE-5 base flow. Instead, significant changes can occur in the streamwise location motivating a TriGlobal analysis approach. TriGlobal analysis solves for three-dimensional disturbance modes. As mentioned earlier, the cost of doing TriGlobal direct methods can be prohibitively expensive and properly applying a pre-conditioner for iterative methods is a challenge unto itself. As a proof-of-concept, TriGlobal analysis has been performed for three-dimensional subdomain located along the centerline of the cone at an approximate location $x/L = 0.4$. Figure 5.4 shows iso-surfaces of the streamwise velocity disturbance. We can see the mode shape highly three-dimensional appears to correspond tot he lifted boundary layer profile along the centerline.

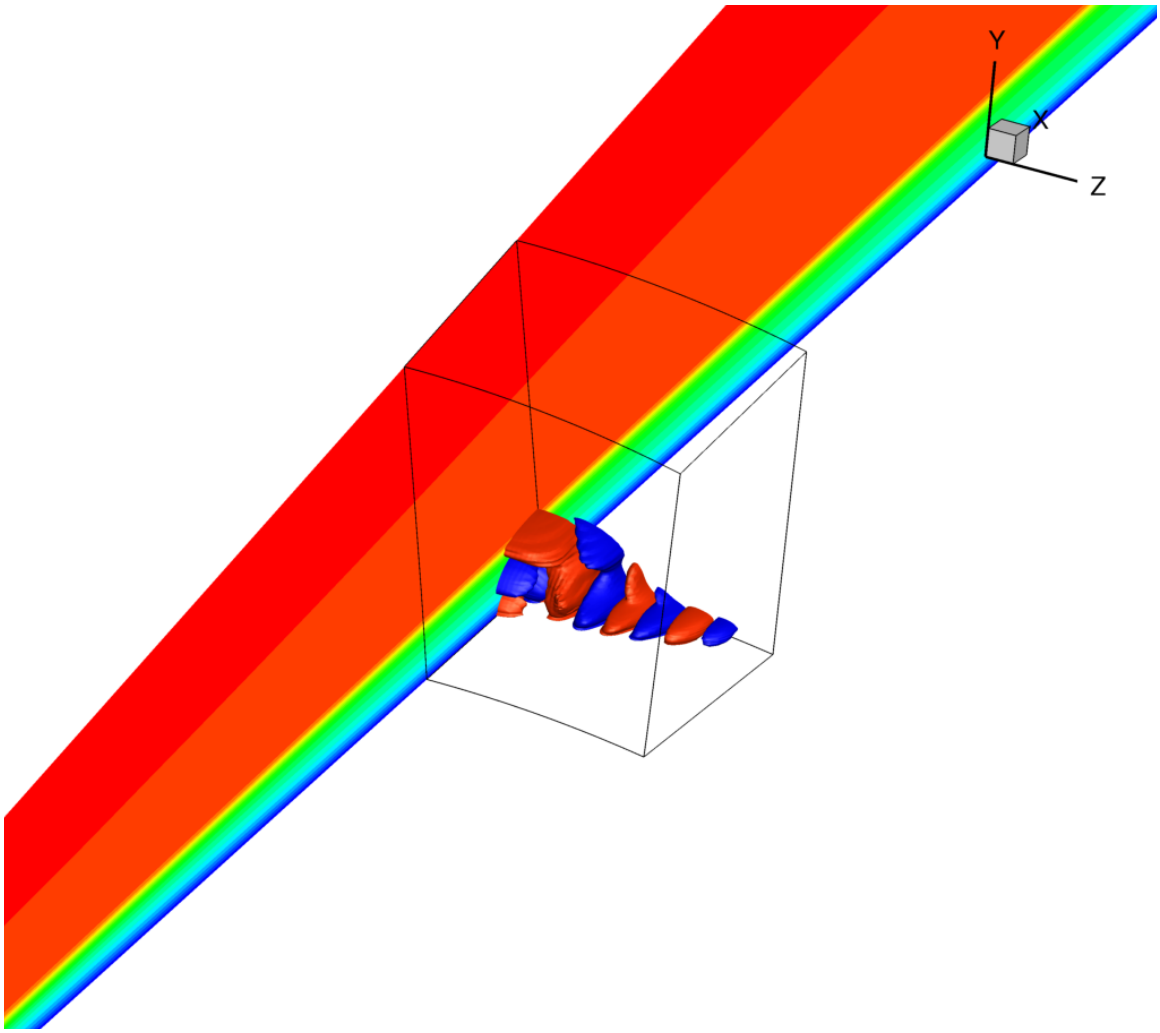

Figure 5.4: Results of TriGlobal analysis for a small sub-domain located along the centerline of the HIFiRE-5 geometry approximately $x/L = 0.4$. Iso-surfaces are of streamwise disturbance velocity.

5.1.2 Input-Output Analysis

With access to the numerical Jacobian, we are able to define the adjoint of the operator as defined in the Appendix section B.1. This allows us to express the disturbance behavior using Input-Output(I/O) formalism from the Appendix section B.4 allowing for additional insight into the behavior of disturbances. Just like the modal methods described in Chapter 2, I/O analysis is based on linearized dynamics of small disturbances. Using the extracted numerical Jacobian technique allows for this methodology to be applied to complex flows as well. Casting the system into an eigenvalue problem for input/output disturbances (Appendices B.4 and B.3, respectively) or applying adjoint looping to converge to an optimal input/output, we can investigate the frequency response of the fluid system.

An unstructured Input-Output analysis tool has been developed to exploit the extracted numerical Jacobian. The software is named Global 3-Dimensional Input-Output analysis (G3DIO) and is part of the US3D software much like GMAUS3D. An I/O analysis using G3DIO has been applied to the unstable frequency for the cylinder flow described in 4. Figure 5.5 (a) and (b) shows the streamwise and spanwise velocity components of the unstable (output) mode. The associated input mode can be seen in figure (c) and (d). This type of analysis shows locations in the flow where the minimal amount of forcing can be applied to achieve the maximum amplification and associated output. While the example case is not physically realizable (i.e. it is not possible to realistically impose the velocity disturbances in the manner that is shown), the capability of this software can be extended to complex flows and input locations restricted to physically relevant regions.

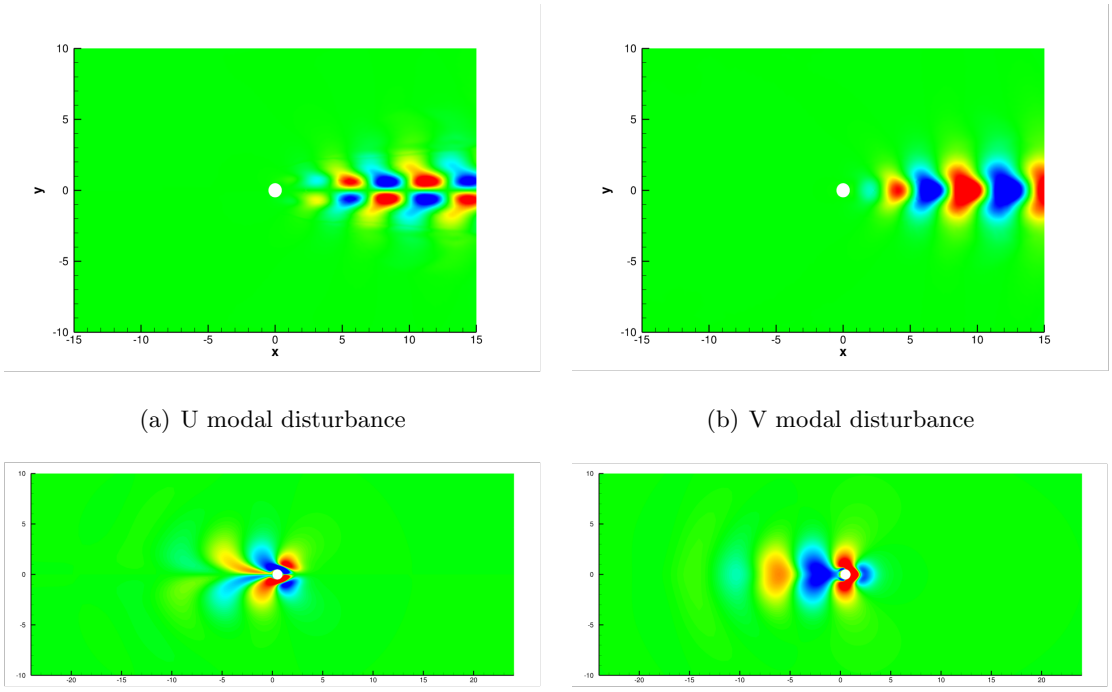

(a) U modal disturbance

(b) V modal disturbance

(c) Input U disturbance

(d) Input V disturbance

Figure 5.5: Input-Output Analysis for unstable cylinder wake mode.

Bibliography

[1] Ryan Gosse, Roger Kimmel, and Heath B Johnson. Study of boundary-layer transition on hypersonic international flight research experimentation 5. *Journal of Spacecraft and Rockets*, 51(1):151–162, January-February 2014.

[2] P Balakumar. Receptivity of a supersonic boundary layer to acoustic disturbances. *AIAA journal*, 47(5):1069–1078, 2009.

[3] P Paredes and V Theofilis. Traveling global instabilities on the hifire-5 elliptic cone model flow. *AIAA Paper*, 75, 2014.

[4] Pedro Paredes, Vassilios Theofilis, D Rodrıguez, and JA Tendero. The pse-3d instability analysis methodology for flows depending strongly on two and weakly on the third spatial dimension. In *6th AIAA Theoretical Fluid Mechanics Conference, Honolulu, HI, June*, pages 27–30, 2011.

[5] Flavio Giannetti, Paolo Luchini, and Luca Marino. Linear stability analysis of three-dimensional lid-driven cavity flow. In *Atti del XIX Congresso AIMETA di Meccanica Teorica e Applicata*, pages 14–17. Aras Edizioni Ancona, Italy, 2009.

[6] Peter K Sweby. High resolution schemes using flux limiters for hyperbolic conservation laws. *SIAM journal on numerical analysis*, 21(5):995–1011, 1984.

[7] Xiaolin Zhong and Xiaowen Wang. Direct numerical simulation on the receptivity, instability, and transition of hypersonic boundary layers. *Annual Review of Fluid Mechanics*, 44:527–561, 2012.

[8] Mark V Morkovin. On the many faces of transition. In *Viscous drag reduction*, pages 1–31. Springer, 1969.

[9] MV Morkovin, E Reshotko, and Th Herbert. Transition in open flow systems-a reassessment. *Bull. Am. Phys. Soc*, 39(9):1882, 1994.

[10] Osborne Reynolds. An experimental investigation of the circumstances which determine whether the motion of water shall be direct or sinuous, and of the law of resistance in parallel channels. *Proceedings of the royal society of London*, 35(224-226):84–99, 1883.

[11] Philip G Drazin and William Hill Reid. *Hydrodynamic stability*. Cambridge university press, 2004.

[12] William M'F Orr. The stability or instability of the steady motions of a perfect liquid and of a viscous liquid. part ii: A viscous liquid. In *Proceedings of the Royal Irish Academy. Section A: Mathematical and Physical Sciences*, pages 69–138. JSTOR, 1907.

[13] Arnold Sommerfeld. Ein beitrag zur hydrodynamischen erklaerung der turbulenten fluessigkeitsbewegungen. In *Proceedings of the 4th International Congress of Mathematicians III, Rome, Italy*, pages 116–124, 1908.

[14] Steven A Orszag. Accurate solution of the orr–sommerfeld stability equation. *Journal of Fluid Mechanics*, 50(04):689–703, 1971.

[15] Geoffrey I Taylor. Stability of a viscous liquid contained between two rotating cylinders. *Philosophical Transactions of the Royal Society of London. Series A, Containing Papers of a Mathematical or Physical Character*, pages 289–343, 1923.

[16] Walter Tollmien. Über die entstehung der turbulenz. 1. mitteilung. *Nachrichten von der Gesellschaft der Wissenschaften zu Göttingen, Mathematisch-Physikalische Klasse*, 1929:21–44, 1928.

[17] Hermann Schlichting. Zur enstehung der turbulenz bei der plattenströmung. *Nachrichten von der Gesellschaft der Wissenschaften zu Göttingen, Mathematisch-Physikalische Klasse*, 1933:181–208, 1933.

[18] PS Klebanoff, KD Tidstrom, and LM Sargent. The three-dimensional nature of boundary-layer instability. *Journal of Fluid Mechanics*, 12(01):1–34, 1962.

[19] LM Mack. The inviscid stability of the compressible laminar boundary layer. *Space Programs Summary*, (37-23):297, 1963.

[20] M Gaster. On the generation of spatially growing waves in a boundary layer. *Journal of Fluid Mechanics*, 22(03):433–441, 1965.

[21] Daniel D Joseph. Stability of fluid motions. i, ii. *NASA STI/Recon Technical Report A*, 77:12423, 1976.

[22] Steven A Orszag and Anthony T Patera. Secondary instability of wall-bounded shear flows. *Journal of Fluid Mechanics*, 128:347–385, 1983.

[23] BJ Bayly. Three-dimensional instability of elliptical flow. *Physical review letters*, 57(17):2160, 1986.

[24] RT Pierrehumbert. Universal short-wave instability of two-dimensional eddies in an inviscid fluid. *Physical review letters*, 57(17):2157, 1986.

[25] Patrick Huerre and Peter A Monkewitz. Local and global instabilities in spatially developing flows. *Annual review of fluid mechanics*, 22(1):473–537, 1990.

[26] FP Bertolotti, Th Herbert, and PR Spalart. Linear and nonlinear stability of the blasius boundary layer. *Journal of Fluid Mechanics*, 242:441–474, 1992.

[27] Chau-Lyan Chang and Mujeeb R Malik. Oblique-mode breakdown and secondary instability in supersonic boundary layers. *Journal of Fluid Mechanics*, 273:323–360, 1994.

[28] AMO Smith and Nathalie Gamberoni. Transition, pressure gradient, and stability theory. report no. es. 26388, douglas aircraft co. *Inc., El Segundo, CA*, 1956.

[29] Helen L Reed, William S Saric, and Daniel Arnal. Linear stability theory applied to boundary layers. *Annual review of fluid mechanics*, 28(1):389–428, 1996.

[30] Matthew P Juniper, Ardeshir Hanifi, and Vassilios Theofilis. Modal stability theorylecture notes from the flow-nordita summer school on advanced instability methods for complex flows, stockholm, sweden, 2013. *Applied Mechanics Reviews*, 66(2):024804, 2014.

[31] Leslie M Mack. Boundary-layer linear stability theory. Technical report, DTIC Document, 1984.

[32] Thorwald Herbert. Parabolized stability equations. *Annual Review of Fluid Mechanics*, 29(1):245–283, 1997.

[33] Lloyd N Trefethen and David Bau III. *Numerical linear algebra*, volume 50. Siam, 1997.

[34] Walter Edwin Arnoldi. The principle of minimized iterations in the solution of the matrix eigenvalue problem. *Quarterly of Applied Mathematics*, 9(1):17–29, 1951.

[35] G. Moretti. The lambda scheme. *Computers and Fluids*, 7(3):191–205, Sept. 1979.

[36] PL Roe. Characteristic-based schemes for the euler equations. *Annual review of fluid mechanics*, 18(1):337–365, 1986.

[37] Joseph L Steger and RF Warming. Flux vector splitting of the inviscid gasdynamic equations with application to finite-difference methods. *Journal of computational physics*, 40(2):263–293, 1981.

[38] Bram Van Leer. Towards the ultimate conservative difference scheme. ii. monotonicity and conservation combined in a second-order scheme. *Journal of computational physics*, 14(4):361–370, 1974.

[39] Carlos D Correa, Robert Hero, and Kwan-Liu Ma. A comparison of gradient estimation methods for volume rendering on unstructured meshes. *IEEE Transactions on Visualization and Computer Graphics*, 17(3):305–319, 2011.

[40] Dimitri Mavriplis. Revisiting the least-squares procedure for gradient reconstruction on unstructured meshes. In *16th AIAA Computational Fluid Dynamics Conference*, page 3986, 2003.

[41] Sung-Eun Kim. A multi-dimensional linear reconstruction scheme for arbitrary unstructured mesh. In *16th AIAA Computational Fluid Dynamics Conference*, page 3990, 2003.

[42] I. N. Nompelis, T. Drayna, and G. V. Candler. Development of a hybrid unstructured implicit solver for the simulation of reacting flows over complex geometries. *AIAA Paper 2004-2227*, 2004.

[43] Robert W MacCormack and Graham V Candler. The solution of the navier-stokes equations using gauss-seidel line relaxation. *Computers & fluids*, 17(1):135–150, 1989.

[44] P. Subbareddy and G. V. Candler. A fully discrete, kinetic energy consistent finite-volume scheme for compressible flows. *Journal of Computational Physics*, 228:1347,1364, 2009.

[45] Michael J Wright, Graham V Candler, and Deepak Bose. Data-parallel line relaxation method for the navier-stokes equations. *AIAA journal*, 36(9):1603–1609, 1998.

[46] Sanjiva K Lele. Compact finite difference schemes with spectral-like resolution. *Journal of computational physics*, 103(1):16–42, 1992.

[47] Eric J Nielsen and William L Kleb. Efficient construction of discrete adjoint operators on unstructured grids using complex variables. *AIAA journal*, 44(4):827–836, 2006.

[48] Kristyn J Maschho and DC Sorensen. A portable implementation of arpack for distributed memory parallel architectures. In *Proceedings of the Copper Mountain Conference on Iterative Methods, April*, pages 9–13, 1996.

[49] Xiaoye S. Li and James W. Demmel. Superludist: A scalable distributed-memory sparse direct solver for unsymmetric linear systems. *ACM Trans. Mathematical Software*, 29(2):110–140, June 2003.

[50] Laura Grigori, James W. Demmel, and Xiaoye S. Li. Parallel symbolic factorization for sparse lu with static pivoting. *SIAM J. Scientific Computing*, 29(3):1289–1314, 2007.

[51] CP Jackson. A finite-element study of the onset of vortex shedding in flow past variously shaped bodies. *Journal of fluid Mechanics*, 182:23–45, 1987.

[52] A Zebib. Stability of viscous flow past a circular cylinder. *Journal of Engineering Mathematics*, 21(2):155–165, 1987.

[53] DC Hill. Adjoint systems and their role in the receptivity problem for boundary layers. *Journal of Fluid Mechanics*, 292:183–204, 1995.

[54] JD Crouch, A Garbaruk, and D Magidov. Predicting the onset of flow unsteadiness based on global instability. *Journal of Computational Physics*, 224(2):924–940, 2007.

[55] Frederick Gwynn Blottner, Margaret Johnson, and Molly Ellis. Chemically reacting viscous flow program for multi-component gas mixtures. Technical report, Sandia Labs., Albuquerque, N. Mex., 1971.

[56] Leslie M Mack. Linear stability theory and the problem of supersonic boundary-layer transition. *AIAA journal*, 13(3):278–289, 1975.

[57] Alexander Fedorov, Vitaly Soudakov, Ivan Egorov, Andrey Sidorenko, Yury Gromyko, Dmitry Bountin, Pavel Polivanov, and Anatoly Maslov. High-speed boundary-layer stability on a cone with localized wall heating or cooling. *AIAA Journal*, 53(9):2512–2524, 2015.

[58] Helen L Reed, Eduardo Perez, Joseph Kuehl, Travis Kocian, and Nicholas Oliviero. Verification and validation issues in hypersonic stability and transition prediction. *Journal of Spacecraft and Rockets*, 52(1):29–37, 2014.

[59] Heath B Johnson and Graham V Candler. Hypersonic boundary layer stability analysis using pse-chem. *AIAA paper*, 5023:35, 2005.

[60] Uwe Ehrenstein and Francois Gallaire. On two-dimensional temporal modes in spatially evolving open flows: the flat-plate boundary layer. *Journal of Fluid Mechanics*, 536:209–218, 2005.

[61] Derek J Dinzl and Graham V Candler. Analysis of crossflow instability on hifire-5 using direct numerical simulation. In *53rd AIAA Aerospace Sciences Meeting*, page 0279, 2015.

[62] Yousef Saad. *Iterative methods for sparse linear systems*. Siam, 2003.

[63] Thomas J Juliano, Laura Paquin, and Matthew P Borg. Measurement of hifire-5 boundary-layer transition in a mach-6 quiet tunnel with infrared thermography. In *54th AIAA Aerospace Sciences Meeting*, page 0595, 2016.

Appendix A

Glossary and Acronyms

Care has been taken in this thesis to minimize the use of jargon and acronyms, but this cannot always be achieved. This appendix defines jargon terms in a glossary, and contains a table of acronyms and their meaning.

A.1 Glossary

- **Mode** – A vector solution to an eigenvalue or singular value problem
- **Linear Stability** – Response of a fluid system to small amplitude disturbances. If the flow is perturbed but returns to its initial state, the fluid system is deemed stable. If the flow is augmented resulting in transition to either turbulence or another, laminar state, the flow is deemed unstable.
- **Transient Growth** – Interaction between two or more decaying modes in a system the results in a brief amplification of disturbance energy.
- **Hessenberg Matrix** – A matrix whose elements below the first subdiagonal are zero.

A.2 Acronyms

Table A.1: Acronyms

Acronym	Meaning
TPS	Thermal Protection System
CFD	Computational Fluid Dynamics
LST	Linear Stability Theory
PSE	Parabolized Stability Equations
EVP	Eigenvalue problem
IBVP	Initial Boundary Value Problem
US3D	Unstructured Solver 3-Dimensional
GMAUS3D	Global Mode Analysis for US3D
G3-DIO	Global 3-Dimensional Input-Output
Mode	Eigenvector resulting from solution of an EVP

Appendix B

Key Aspects of Non-Modal Analysis

B.1 Definition of Adjoint

Formal definition of Adjoints

Starting with the linear system of equations,

$$\psi_t = \mathcal{A}\psi + \mathcal{B}d$$
$$\phi = \mathcal{C}\psi$$

which define an input forcing of d onto the state-space vector ψ, and a measured output vector *phi*. Here $\mathcal{B}$ maps input disturbances d onto the state-space. The linear evolution state-space vector *psi* evolves according to the linear system $\psi_t = \mathcal{A}\psi$, and $\mathcal{C}$ maps state-space variables to an output.

It is useful to think of the operators $\mathcal{A}, \mathcal{B}, \mathcal{C}$ as projection operators between the state, input, and output spaces. More formally,

$$\mathcal{A}: S_\psi \to S_\psi$$
$$\mathcal{B}: S_d \to S_\psi$$
$$\mathcal{C}: S_\psi \to S_\phi$$

are the forward mappings between spaces. Whereas,

$$\mathcal{A}^\dagger: S_\psi \to S_\psi$$
$$\mathcal{B}^\dagger: S_\psi \to S_d$$
$$\mathcal{C}^\dagger: S_\phi \to S_\psi$$

are backward mappings (adjoint operators).

If we define an operator as the projection from some space to another, (say $1 \to 2$) then the adjoint of that operator is the reverse projection (as in $2 \to 1$). The formal definition of an adjoint requires the use of a norm.

$$\mathcal{A}^\dagger : \langle \psi_1, \mathcal{A}\Psi_2 \rangle_{S_\psi} = \left\langle \mathcal{A}^\dagger \psi_1, \psi_2 \right\rangle_{S_\psi}$$
$$\mathcal{B}^\dagger : \langle \psi, \mathcal{B}d \rangle_{S_\psi} = \left\langle \mathcal{B}^\dagger \psi, d \right\rangle_{S_d}$$
$$\mathcal{C}^\dagger : \langle \phi, \mathcal{C}\phi \rangle_{S_\phi} = \left\langle \mathcal{C}^\dagger \phi, \psi \right\rangle_{S_\psi}$$

The definition of a norm/inner-product requires some sort of inner product operator. For example,

$$\langle \psi_1, \psi_2 \rangle_{S_\psi} = \int_V \psi_1^*(\mathbf{x}) \mathcal{Q}_\psi \psi_2(\mathbf{x}) d\mathbf{x}$$

Where $\mathcal{Q}_\psi$ is the inner-product matrix and will be different depending on the choice of the norm (i.e. L_2, Mack-Energy, etc..)

Discrete Adjoints

Let us now define the discrete operators of $\mathcal{A}$, $\mathcal{B}$, and $\mathcal{C}$ as A, B, and C respectively. What are $A^\dagger$, $B^\dagger$, and $C^\dagger$? Numerically we can write,

$$\begin{aligned} \text{A: } \langle \psi_1, A\psi_2 \rangle_{S_\psi} &= \left\langle A^\dagger \psi_1, \psi_2 \right\rangle_{S_\psi} \\ \psi_1 Q_\psi A \psi_2 &= \left(A^\dagger \psi_1 \right)^* Q_\psi \psi_2 \\ &= \psi_1^* \left(A^\dagger \right)^* Q_\psi \psi_2 \end{aligned}$$

or,

$$\psi_1 Q_\psi A \psi_2 = \psi_1^* \left(A^\dagger \right)^* Q_\psi \psi_2$$

This relationship must hold for all ψ_1 and ψ_2. so,

$$Q_\psi A = \left(A^\dagger \right)^* Q_\psi \;\rightarrow\; Q_\psi A Q_\psi^{-1} = \left(A^\dagger \right)^* \;\rightarrow\; \boxed{A^\dagger = Q_\psi^{-1} A^* Q_\psi}$$

similarly,

$$\begin{aligned} B^\dagger\text{: } \psi^* Q_\psi B d = \psi^* \left(B^\dagger \right)^* Q_d d \;\rightarrow\; \boxed{B^\dagger = Q_d^{-1} B^* Q_\psi} \\ C^\dagger\text{: } \phi^* Q_\phi C \psi = \phi^* \left(C^\dagger \right)^* Q_\psi \psi \;\rightarrow\; \boxed{C^\dagger = Q_\psi^{-1} C^* Q_\phi} \end{aligned}$$

The full derivation of $B^\dagger$ and $C^\dagger$ is left as an exercise to the reader.

B.2 Eigenvalues vs. Singular Values

Eigenvalues and singular values are important mathematical properties of dynamical operators. Proper understanding of the basic concepts is necessary when considering

modal and nonmodal analysis of linear global operators. This section is dedicated to explaining in brief the similarities and differences between eigenvalues and singular values. Only square matrices will be considered in this section in hopes of keeping the discussion relatively simple.

B.2.1 Eigenvalues and Eigenvectors

An *eigenvector* and *eigenvalue* of a square matrix A can be defined as a scalar λ and a nonzero vector x such that;

$$Ax = \lambda x$$

When the matrix describes a transformation from one vector space onto itself, the eigenvalue can play an important roll in describing the behavior of a vector undergoing this transformation. Additionally, as seen above, there is no requirement that the eigenvector be normalized.

Furthermore, we can rewrite the original eigenvalue equation as

$$(A - \lambda I)\, x = 0, \qquad x \neq 0.$$

The above equation implies that $(A - \lambda I)$ is singular and thus;

$$\det (A - \lambda I) = 0.$$

This expression now only relates the matrix and its eigenvalue through the determinant. This is known as the *characteristic equation* or *characteristic polynomial* of A.

B.3 Non-normal Matrices

Recall that any matrix may be decomposed into unitary matrices and a diagonal of corresponding amplifications of each unitary vector via the singular value decomposition (SVD) as,

$$A = U\Sigma V^*$$

Taking the product of A with its adjoint $A^\dagger$ yields an eigenvalue problem for output modes,

$$\begin{aligned} AA^\dagger &= (U\Sigma V^*)\,(U\Sigma V^*)^\dagger \\ &= (U\Sigma V^*)\,(V\Sigma U^*) \\ &= U\Sigma V^* V\Sigma U^* \\ &= U\Sigma\Sigma U^* \end{aligned}$$

Noting that U and V are unitary matricies and the product of each with their complex conjugate transpose results in the identity matrix. After right multiplying the above by U we get,

$$AA^\dagger U = U\Sigma\Sigma$$

For each eigenvector of the resulting eigensystem we can write,

$$\boxed{AA^\dagger u_i = \sigma^2 u_i}$$

Similarly we can write the reverse as,

$$\boxed{A^\dagger A v_i = \sigma^2 v_i}$$

which yields the input modes. This allows us to solve for input and output disturbances using similar methodologies as those imposed in modal analysis.

B.4 Input-Output Analysis

The following section shows the mathematical formulation of input-output analysis for dynamical systems. This section derives and explains how to perform input-output analysis using a linear system theory approach.

B.4.1 Mathematical Formulation

Consider a dynamical system defined by,

$$\psi_t = \mathcal{A}\psi(t)$$

where, $\psi_t = \frac{\partial \psi(t)}{\partial t}$ is the evolution of our field, $\mathcal{A}$ is our propagator operator, and $\psi(t)$ is our field at time t. Now suppose we wish to add forced disturbances to our state space with a time dependent forcing function d with the goal to observe some measured output of our field ψ. We can define two equations,

$$\psi_t = \mathcal{A}\psi + \mathcal{B}d$$
$$\phi = \mathcal{C}\psi$$

where, $\mathcal{B}$ transforms input disturbances into the state-space, ϕ is our desired measured quantity with $\mathcal{C}$ being the transformation of our state-space variables to our output.

Let us assume a modal form of our state space ψ, forcing inputs d, and output field ϕ

$$\psi(x, y, z, t) = \hat{\psi}(x, y, z)\text{Exp}\left[\text{i}\omega t\right]$$
$$d(t) = \hat{d}(\text{i}\omega)\text{Exp}\left[\text{i}\omega t\right]$$
$$\phi(t) = \hat{\phi}(\text{i}\omega)\text{Exp}\left[\text{i}\omega t\right]$$

The resulting state-space and output equations becomes,

$$\mathrm{i}\omega\hat{\psi} = \mathcal{A}\hat{\psi} + \mathcal{B}\hat{d}(\mathrm{i}\omega)$$

$$\downarrow$$

$$(\mathrm{i}\omega\mathcal{I} - \mathcal{A})\,\hat{\psi} = \mathcal{B}\hat{d}$$

and,

$$\hat{\phi}(\mathrm{i}\omega) = \mathcal{C}\hat{\psi}(\mathrm{i}\omega)$$

where $\mathcal{I}$ is the identity matrix.

If we combine these two equations we end up with,

$$\hat{\phi} = \mathcal{C}\,(\mathrm{i}\omega\mathcal{I} - \mathcal{A})^{-1}\,\mathcal{B}\hat{d}$$

which is one equation for output variables ϕ based on our state-space resolvent $(\mathrm{i}\omega\mathcal{I} - \mathcal{A})^{-1}$, and our input forcing function $\hat{d}$. The term $\mathcal{C}\,(\mathrm{i}\omega\mathcal{I} - \mathcal{A})^{-1}\,\mathcal{B}$ can be thought of as a single operator taking inputs $\hat{d}$ and mapping them to outputs $\hat{\phi}$. This is known as the transfer function H,

$$\boxed{H(\mathrm{i}\omega) = \mathcal{C}\,(\mathrm{i}\omega\mathcal{I} - \mathcal{A})^{-1}\,\mathcal{B}}$$

which is the mapping from our input-space to our output space,

$$H(\mathrm{i}\omega) : S_d \to S_\phi$$

Whereas the $H^\dagger$ is defined as,

$$H^\dagger(\mathrm{i}\omega) = \mathcal{B}^\dagger\left(-\mathrm{i}\omega\mathcal{I} - \mathcal{A}^\dagger\right)^{-1}\mathcal{C}^\dagger$$

or

$$\boxed{H^\dagger(\mathrm{i}\omega) = -\mathcal{B}^\dagger\left(\mathrm{i}\omega\mathcal{I} + \mathcal{A}^\dagger\right)^{-1}\mathcal{C}^\dagger}$$

and is the mapping from output-space to the input-space,

$$H^\dagger(\mathrm{i}\omega) : S_\Phi \to S_d$$

A formal definition of operators and their adjoint can be found in Appendix B.1. Using the definition of adjoint operators and associate norms allows for the solution of global modes associated to the transfer function H. Exploiting the mathematical characteristics of non-normal matrices (see Appendix B.3,the composition of $H(\mathrm{i}\omega)H^\dagger(\mathrm{i}\omega)$ results in,

$$\begin{aligned}
H(\mathrm{i}\omega)H^\dagger(\mathrm{i}\omega) &= \left(C\left(\mathrm{i}\omega I - A\right)^{-1}B\right)\left(-B^\dagger\left(\mathrm{i}\omega I + A^\dagger\right)^{-1}C^\dagger\right) \\
&= \left(C\left(\mathrm{i}\omega I - A\right)^{-1}B\right)\left(-Q_d^{-1}B^*Q_\psi\left(\mathrm{i}\omega I + Q_\psi^{-1}A^*Q_\psi\right)^{-1}Q_\psi^{-1}C^*Q_\phi\right) \\
&= \left(C\left(\mathrm{i}\omega I - A\right)^{-1}B\right)\left(-Q_d^{-1}B^*Q_\psi Q_\psi^{-1}\left(\mathrm{i}\omega I + A^*\right)^{-1}Q_\psi Q_\psi^{-1}C^*Q_\phi\right) \\
&= \left(C\left(\mathrm{i}\omega I - A\right)^{-1}B\right)\left(-Q_d^{-1}B^*\left(\mathrm{i}\omega I + A^*\right)^{-1}C^*Q_\phi\right)
\end{aligned}$$

Note that

$$H(\mathrm{i}\omega) = \left(C\left(\mathrm{i}\omega I - A\right)^{-1}B\right) \tag{B.1}$$

and

$$H^*(\mathrm{i}\omega) = \left(B^*\left(-\mathrm{i}\omega I - A^*\right)^{-1}C^*\right) \tag{B.2}$$

Depending on the order in which we construct the inner product between the transfer function H and its adjoint $H^\dagger$ results in eigenvalue systems for input or output global modes.

$$\boxed{H(\mathrm{i}\omega)H^\dagger(\mathrm{i}\omega) = H(\mathrm{i}\omega)Q_d^{-1}H^*(\mathrm{i}\omega)Q_\phi} \tag{B.3}$$

$$\boxed{H^{\dagger}(\mathrm{i}\omega)H(\mathrm{i}\omega) = H^{*}(\mathrm{i}\omega)Q_{\phi}H(\mathrm{i}\omega)Q_{d}^{-1}} \tag{B.4}$$

The analysis is considered to be a nonmodal approach since the construction of the either system ($H^{\dagger}H$ or $HH^{\dagger}$) and the solution of which results in the eigenvalues (which in this case are the squared singular values) for the state space operator A (the global linear operator). Additionally, by augmenting the mapping matrices (B and C, respectively), we are able to analyze the linear dynamics of the fluid system based on componentwise inputs and outputs (i.e. forcing/response of individual fluid quantities such as mass, momentum, or energy). This will result in a mechanism approach to the stability of the system.

Appendix C

Comparison of Discretization

C.0.2 Discretization and Disturbance Form

We can either employ the finite volume formulation, linearize the equations, and then assume a modal form for our disturbances, or we can linearize the equations about some base state, assume a modal form for the disturbance, and then employ a finite volume discretization. We shall take a moment to go over each implementation and discuss the consequences of each.

Modal Form of Discretization

For the first case, we will first apply the finite volume formulation of the equations. This is done by writing Eqn 3.1 in integral form.

$$\int_V \frac{\partial U_i}{\partial t} dV + \int_V \frac{\partial F_i}{\partial x_j} dV = 0 \tag{C.1}$$

Employing the divergence theorem will change the volume integral of the flux function into a surface integral. we get,

$$\int_V \frac{\partial U_i}{\partial t} dV + \oint_S F_i \cdot dS = 0 \tag{C.2}$$

This represents changes in inside a volume over time are the results of fluxes across its surface. We can now discretize the surface which changes the integral to a sum of fluxes across faces of our computational cell. The volume integral for the time derivative results in a volume average quantity U.

$$V_i \frac{\partial U_i}{\partial t} + \sum_{faces} F_i \cdot S = 0 \tag{C.3}$$

$$V_i \frac{\partial \bar{U}_i}{\partial t} + V_i \frac{\partial U_i'}{\partial t} + \sum_{faces} F_i(\bar{U} + U') \cdot S = 0 \tag{C.4}$$

$$V_i \frac{\partial \bar{U}_i}{\partial t} + V_i \frac{\partial U_i'}{\partial t} + \sum_{faces} \left[F_i(\bar{U}) + \frac{\partial F(U)}{\partial U} U' \right] \cdot S = 0 \tag{C.5}$$

$$V_i \frac{\partial U_i'}{\partial t} + \sum_{faces} \frac{\partial F(U)}{\partial U} U' \cdot S = 0 \tag{C.6}$$

$$V_i \frac{\partial U_i'}{\partial t} + \sum_{faces} A\ U' \cdot S = 0 \tag{C.7}$$

$$V_i \frac{\partial U_i'}{\partial t} + \sum_{faces} \left(A^+\ U_{cl}' + A^- U_{cr}' \right) \cdot S = 0 \tag{C.8}$$

$$V_i\ \mathrm{i}\ \omega\ \hat{U}_i + \sum_{faces} \left(A^+\ \hat{U}_i + A^- \hat{U}_{ii} \right) \cdot S = 0 \tag{C.9}$$

Discretization of Modal Form

The result of applying a modal assumption to the discretized equations resulted in the following equation,

$$V_i\ \mathrm{i}\ \omega\ \hat{U}_i + \sum_{faces} \left(A^+\ \hat{U}_i + A^- \hat{U}_{ii} \right) \cdot S = 0 \tag{C.10}$$

We can compare this result obtained by first assuming a modal form of the continuous equations and then applying the finite volume discretization. For this approach, we will first take the continuous equations and linearize them about some base state to obtain our disturbance equations. This is done by expanding our equation into a base state plus some small perturbation quantity, i.e $U = \bar{U} + U'$.

$$\frac{\partial \bar{U}_i}{\partial t} + \frac{\partial U_i'}{\partial t} + \frac{\partial F_i(\bar{U} + U')}{\partial x_j} = 0 \tag{C.11}$$

We can express $F(\bar{U} + U')$ via Taylor Series expansion about the base state. We will neglect the nonlinear terms.

$$F(\bar{U} + U') = F(\bar{U}) + \frac{\partial F(\bar{U})}{\partial U} U' + \mathcal{O}^2 \tag{C.12}$$

Performing similar expansion for the rest of the flux vectors we arrive at,

$$\frac{\partial \bar{U}}{\partial t} + \frac{\partial U'}{\partial t} + \frac{\partial F(\bar{U})}{\partial x_j} + \frac{\partial}{\partial x_j}\left[\frac{\partial F(\bar{U})}{\partial U} U'\right] = 0 \tag{C.13}$$

Subtracting off the base state and rearranging results in linearized equation for disturbances in compressible flows.

$$\frac{\partial U'}{\partial t} + \frac{\partial}{\partial x_j}\left[\frac{\partial F(\bar{U})}{\partial U} U'\right] = 0 \tag{C.14}$$

Assuming a modal form $U = \hat{U}\exp[\sigma]$ and replacing $\frac{\partial F(\bar{U})}{\partial U} = A'$

$$\mathrm{i}\ \omega\ \hat{U}\exp[\sigma] + \frac{\partial}{\partial x_j}\left[A'\hat{U}\exp[\sigma]\right] = 0 \tag{C.15}$$

$$\int_V \mathrm{i}\ \omega\ \hat{U}\exp[\sigma]\, dV + \int_V \frac{\partial}{\partial x_j}\left[A'\ \hat{U}\exp[\sigma]\right] dV = 0 \tag{C.16}$$

$$\int_V \mathrm{i}\ \omega\ \hat{U}\ dV + \int_V \frac{\partial}{\partial x_j}\left[A'\ \hat{U}\right] dV = 0 \tag{C.17}$$

$$V\ \mathrm{i}\ \omega\ \hat{U} + \oint_S \left(A'\ \hat{U}\right)\cdot dS = 0 \tag{C.18}$$

$$V\ \mathrm{i}\ \omega\ \hat{U} + \sum_{faces}\left(A'\ \hat{U}\right)\cdot S = 0 \tag{C.19}$$

$$V_i \; \mathrm{i} \; \omega \; \hat{U}_i + \sum_{faces} \left(A^{+} \; \hat{U}_i + A^{-} \hat{U}_{ii} \right) \cdot S = 0 \tag{C.20}$$